Depinning and dynamics of vortices confined in mesoscopic flow channels.

R. Besseling* and P.H. Kes

*Kamerlingh Onnes Laboratorium, Leiden University,
P.O. Box 9504, 2300 RA Leiden, the Netherlands.*

T. Dröse

I. Institut für Theoretische Physik, Universität Hamburg, Jungiusstrasse 9, D-20355 Hamburg, Germany.[†]

V.M. Vinokur

Materials Science Division, Argonne National Laboratory, Argonne, Illinois 60439
(Dated: February 2, 2008)

We study numerically and analytically the behavior of vortex matter in artificial flow channels confined by pinned vortices in the channel edges (CE's). The critical current density J_s for channel flow is governed by the interaction with the static vortices in the CE's. Motivated by early experiments which showed oscillations of J_s on changing (in)commensurability between the channel width w and the natural vortex row spacing b_0, we study structural changes associated with (in)commensurability and their effect on J_s and the dynamics. The behavior depends crucially on the presence of disorder in the arrays in the CE's. For ordered CE's, maxima in J_s occur at commensurability $w = nb_0$ (n integer), while for $w \neq nb_0$ defects *along* the CE's cause a vanishing J_s. For weak disorder, the sharp peaks in J_s are reduced in height and broadened via nucleation and pinning of defects. The corresponding structures in the channels (for zero or weak disorder) are quasi-1D n row configurations, which can be adequately described by a (disordered)sine-Gordon model. For larger disorder, matching between the longitudinal vortex spacings in and outside the channel becomes irrelevant and, for $w \simeq nb_0$, the shear current J_s levels at $\sim 30\%$ of the value J_s^0 for the ideal commensurate lattice. Around 'half filling' ($w/b_0 \simeq n \pm 1/2$) the disorder leads to new phenomena, namely stabilization and pinning of *misaligned* dislocations and coexistence of n and $n \pm 1$ rows in the channel. At sufficient disorder, these quasi-2D structures cause a *maximum* in J_s around mismatch, while J_s smoothly decreases towards matching due to annealing of the misaligned regions. Near threshold, motion inside the channel is always plastic. We study the evolution of static and dynamic structures on changing w/b_0, the relation between the J_s modulations and transverse fluctuations in the channels and find dynamic ordering of the arrays at a velocity with a matching dependence similar to J_s. We finally compare our numerical findings at strong disorder with recent mode-locking experiments, and find good qualitative agreement.

Contents

*Presently at the School of Physics, University of Edinburgh, Kings Buildings, Mayfield Road, Edinburgh EH9 3JZ, United Kingdom
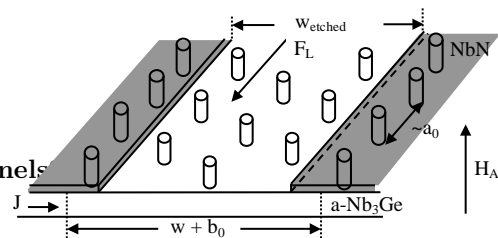[†]Presently at Siemens AG, St.-Martin-Str. 76, D-81617 München, Germany

FIG. 1: Sketch of the artificial channel geometry. In the gray areas vortices are pinned by the strong-pinning NbN layer while inside the channels pinning due to material inhomogeneities is negligible. The etched channel width w_{etched} (of the order of a few row spacings b_0) and the effective width w are indicated.

I. INTRODUCTION

The depinning and dynamics of the vortex lattice (VL) in type II superconductors is exemplary for the behavior of driven, periodic media in presence of a pinning potential [1]. Other examples range from sliding surfaces exhibiting static and dynamic friction and absorbed monolayers [3] to charge density waves (CDW's) [2], Wigner crystals [4] and (magnetic) bubble arrays [5]. Vortex matter offers the advantage that the periodicity a_0 of the hexagonal lattice can be tuned by changing the magnetic induction B. In addition, the effect of various types of pinning potentials can be studied. This pinning potential, arising from inhomogeneities in the host material, can be completely random, as in most natural materials, or can be arranged in periodic arrays using nanofabrication techniques [6, 7]. In a variety of cases correlated inhomogeneities occur naturally in a material, such as twin boundaries and the layered structure of the high T_c superconductors [8].

Depinning of the VL in a *random potential* generally involves regions of plastic deformations [9, 10, 11, 12, 13], i.e. coexistence of (temporarily) pinned domains with moving domains. For very weak pinning the typical domain size can exceed the correlation length R_c of the VL (see [11]) and the weak collective pinning theory [14] can be successfully used to estimate the critical current density J_c [15, 16]. However, as either the ratio of the VL shear modulus c_{66} and the elementary pinning strength or the number of pins per correlated volume decreases, plastically deformed regions start to have a noticeable effect on J_c. Recent imaging experiments [17] have shown directly that the rise in J_c in weak pinning materials near the upper critical field B_{c2}, known as the peak effect [15, 16], originates from such, rather sudden, enhancement of the defect density. This strong reduction of the VL correlation length is also accompanied by a qualitative change in the nature of depinning: for strong pinning, depinning proceeds through a dense network of quasi-static flow channels (filaments) such that the typical width of both static and moving 'domains' has approached the lattice spacing [9, 10, 18, 19]. Depinning transitions via a sequence of static, channel like structures have also been observed experimentally via transport experiments [20].

In superconductors with *periodic* pinning arrays (PPA's), matching effects between the lattice and the PPA become important. As shown first by Daldini and Martinoli [21, 22], when the vortex spacing coincides with the periodicity of the potential, pronounced maxima can occur in J_c, while at mismatch defects (discommensurations) appear which gives rise to a reduced J_c. The last decade, many more studies of VL's in PPA's have appeared, both experimentally and numerically. Pronounced commensurability effects were found in films with 2-D periodic pinning [6, 7, 23] for flux densities equal to (integers of) the density of dots. In these systems, vortex chains at interstitial positions of the periodic arrays (e.g. at the second matching field of a square pinning array) can exhibit quasi one-dimensional motion under the influence of the interaction with neighboring, pinned vortices [24], as has also been observed in numerical simulations [25]. In addition these simulations have revealed that, depending on the vortex interactions and the symmetry or strength of the PPA, a rich variety of other states and dynamic transitions can occur, often leading to peculiar transport characteristics.

Besides the above examples, the phenomenon of vortex channelling can also arise from the presence of grain boundaries in the sample. Historically, the 'shear' depinning of vortices in grain boundaries in low T_c materials received considerable attention [26, 27] because it could explain the quadratic decrease of J_c near B_{c2} in practically relevant poly-crystalline superconductors. More recently, the interesting issue of channelling of mixed Abrikosov-Josephson vortices in grain boundaries in high T_c materials was addressed in detail by Gurevich [28].

A system in which channel motion and its dependence on the structural properties of vortex matter can be studied systematically is that of narrow, weak pinning flow channels in a superconducting film [29], see Fig. 1. The samples are fabricated by etching straight channels of width $w_{etched} \gtrsim 100$ nm through the top layer of an a-NbGe/NbN double layer. With a magnetic field applied perpendicular to the film, vortices penetrate both the strong pinning NbN in the channel edges (CE's) and the remaining NbGe weak pinning channels. The strongly
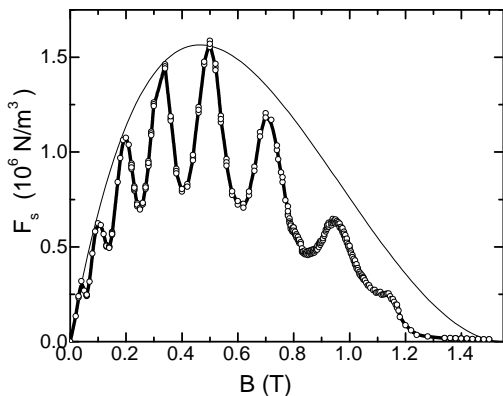
FIG. 2: Data: critical shear force density $F_s = J_s B$, determined using a velocity criterion $v/a_0 \approx 1$ MHz, versus applied field for a channel sample with $w_{etched} \approx 230$ nm at $T = 1.94$ K. Drawn line: Eq.(1) with $A = 0.05$, $B_{c2} = 1.55$ T, $\lambda(T) = 1.13$ μm and effective width $w = 300$ nm.

pinned CE vortices provide confinement to the vortices inside the channel as well as the pinning (shear) potential which opposes the Lorentz force from a transport current J applied perpendicular to the channel. By changing the applied field H one can tune the commensurability between the vortex lattice constants and the channel width, allowing a detailed study of the shear response and threshold for plastic flow as a function of the mismatch and the actual microstructure in the channel.

Phenomenologically, plastic flow in the channel occurs when the force density $F = JB$ (with B/Φ_0 the vortex density) exceeds $2\tau_{max}/w$, where $\tau_{max} = Ac_{66}$ is the flow stress at the edge (the factor 2 is due to both CE's) and w is the effective width between the first pinned vortex rows, defined in Fig. 1. Thus, the critical force density is given by:

$$F_s = J_s B = 2Ac_{66}/w. \qquad (1)$$

The parameter A describes microscopic details of the system: it depends on lattice orientation, (an)harmonicity of the shear potential, details of the vortex structure in the CE's and the microstructure of the array inside the channel. Critical current measurements as function of applied field reflected this change in microstructure through oscillations of F_s, shown in Fig. 2 for a channel with $w_{etched} \approx 230$ nm. Note that in such a narrow channel, the pinning strength due to intrinsic disorder in the a-NbGe is at most 10% of F_s (except for $B \lesssim 50$ mT) and does not affect the oscillations. Since the natural row spacing of the VL is $b_0 = \sqrt{3}a_0/2$, with $a_0^2 = 2\Phi_0/\sqrt{3}B$, and in our geometry $B \simeq \mu_0 H$ one can check that the periodicity of the oscillations corresponds to transitions from $w = nb_0$ to $w = (n \pm 1)b_0$ with n integer, i.e. the principal lattice vector $\vec{a}_0$ is oriented along the channel (Fig. 1). The envelope curve represents Eq.(1) with Brandt's expression for the VL shear modulus [30]:

$$c_{66} = \frac{\Phi_0 B_{c2}}{16\pi\mu_0\lambda^2}b(1-b)^2(1 - 0.58b + 0.29b^2), \qquad (2)$$

($b = B/B_{c2}$ is the reduced field and λ is the penetration depth) and a value $A = 0.05$. This value for A is close to the value $\sqrt{\langle u^2 \rangle}/a_0 = 0.047$ for the relative displacements at the crossover from elastic to plastic deformations as obtained from measurements on the peak effect [16, 17]. This led to a qualitative interpretation of the reduction of F_s at minima as being due to defects in the channel, which develop at incommensurability. However, recent developments [31, 32, 33, 34] have shown that (strong) structural disorder may be present in the CE arrays, in which case the interpretation can drastically differ.

In this article we present numerical and analytical studies of the threshold force and dynamics of vortices in the channel system for various degrees of edge disorder. In an early paper [35] we studied the commensurability effects in the idealized case with periodic arrays in the CE's. In this situation F_s at matching ($w = nb_0$) is equal to the ideal lattice strength $2A^0 c_{66}/w$ (the value $A^0 = 1/(\pi\sqrt{3})$ follows from Frenkels considerations [36]), while at mismatch dislocations develop, leading to $A \simeq 0$. The resulting series of delta-like peaks in F_s versus matching parameter differed considerably from the experimental results, which could not be explained by thermal fluctuations or intrinsic disorder inside the channel. Therefore we investigated the effect of positional disorder in the CE arrays on F_s near commensurability ($w \approx nb_0$) [33]. In this regime the behavior is dominated by the longitudinal displacements of vortices in the chains, i.e. quasi one-dimensional (1D), and F_s is controlled by defects with Burgers vector along the channel. At weak disorder, we found a clear reduction of F_s at commensurability caused by nucleation of defects at threshold, while the existing defects at incommensurability become pinned by disorder, leading to an increase of F_s in the mismatching case.

The present paper first describes in detail these quasi 1D phenomena near commensurability and/or for weak disorder. Using a generalized sine-Gordon model, we quantitatively describe how the structure and transport properties depend on the vortex interaction range and on weak disorder in the CE's. Besides the connection to our system, these results also provide a background for understanding quasi-1D vortex states and matching effects in artificial PPA's, including the effects of disorder which these PPA's may contain due to fabrication uncertainties.

The 1D model shows that, above a certain disorder strength, spontaneously (disorder) induced defects along the CE's dominate over incommensurability induced defects. The commensurability peak in F_s is then completely smeared out with a value of F_s at matching ($w = nb_0$) saturating at $\sim$ 30% of the ideal lattice strength. In the more general case of wider channels, the *transverse* degrees of freedom, especially away from matching ($w/b_0 \simeq n \pm 1/2$), lead to new phenomena: under the influence of disorder, the channel array may split up in regions with n and $n \pm 1$ rows, involving disloca-

tions with Burgers vector strongly *misaligned* with the CE's. At sufficient disorder strength, such dislocations lead to a more effective pinning of the array then the 'aligned' dislocations around matching. F_s then exhibits a smooth oscillation as function of w/b_0, similar to Fig. 2, with yield strength maxima occurring *around mismatch.* This behavior resembles the classical peak effect, i.e. at mismatch the enhanced ability of the arrays to sample configuration space allows better adjustment to the random CE's. In the last part of the paper we show detailed simulations of both static and dynamical aspects of this behavior, including a study of reordering phenomena at large drive. We find an ordering velocity of the arrays with a channel width dependence similar to that of the threshold force. Using a modified version of the dynamic ordering theory in [37] it is shown that such behavior can be explained by a reduction of the energy for formation of misaligned defect pairs away from matching. The numerical results at strong disorder are also in good qualitative agreement with recent mode-locking experiments on the channel system [31, 32].

The outline of the paper is as follows. In Sec.II the channel geometry and the simulation procedure are discussed. The first part of the paper deals with channels having hexagonal, ordered arrays in the CE's: in Sec.III we present the sine-Gordon description and numerical results for a single 1D vortex chain in an ordered channel; in section IV we show how the 1D behavior extends to wider channels with multiple rows and ordered CE's. The second part of the paper deals with disordered channels: section V describes the effects of weak CE disorder on the behavior of a 1D chain, both analytically and using numerical simulations. The effects of weak disorder in wider channels are discussed in Sec.VI. Section VII describes the static and dynamic properties of wider channels in presence of strong disorder, including an analysis of the reordering phenomena in this situation. A comparison with the dynamic ordering theory, the confrontation with experiments and a summary of the results are presented in Secs.VIII and IX.

II. MODEL AND NUMERICAL PROCEDURE

We consider straight vortices at $T = 0$ in the geometry as illustrated in Fig. 3 for the case of 1 row in the channel. The approximation $T = 0$ is well justified over a considerable range of the experiments (see Sec.VIII). The CE's are formed by two semi-infinite static arrays. The distance between the first vortex rows on both sides of the channel is $w + b_0$, with w the *effective* channel width. The vortices are assumed to be fixed by columnar pins in the CE's. The principal axis of the pinned arrays is along the channel direction x. A relative shift Δx is allowed between the arrays. In (a) the simplest configuration is shown, where CE vortices form a perfect triangular lattice. For $\Delta x = 0$, their coordinates are:

$$\mathbf{r}_{n,m} = ([n + frac(m/2)]a_0, m[b_0 + (w - b_0)/2|m|]), \quad (3)$$
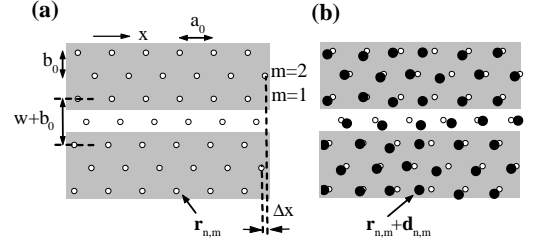

FIG. 3: Channel geometry with pinned vortices in the gray areas. The specific case of $w \simeq b_0$, i.e. with 1 row in the channel is illustrated. (a) Ordered situation: the equilibrium positions $\mathbf{r}_{n,m}$ of pinned vortices in the CE's are denoted by (○). The effective width w and relative shift Δx are indicated. (b) Disordered case. The randomized vortex positions are denoted by (●).

for $m \neq 0$ and $frac(m/2)$ denotes the remainder of $m/2$.

Disorder is incorporated in the model by adding random shifts $\mathbf{d}$ to the coordinates of the ordered arrays:

$$\mathbf{R}_{n,m} = \mathbf{r}_{n,m} + \mathbf{d}_{n,m}, \quad (4)$$

as shown in Fig. 3(b). The amplitudes of the random shifts are characterized by disorder parameters Δ_x and Δ_y as follows: transverse relative displacements d^y/a_0 are chosen independently from a box distribution $[-\Delta_y, \Delta_y]$. The longitudinal shifts $d^x_{n,m}$ are chosen such that the *strain* $(d_{n+1} - d_n)/a_0$ along the channel is uniformly distributed in the interval $[-\Delta_x, \Delta_x]$. The latter provides a simple way of implementing loss of long range order along the CE's. For Δ_x and Δ_y we study the following specific cases: $\Delta_x, \Delta_y = 0$ in Secs. III,IV, $\Delta_x \equiv \Delta, \Delta_y = 0$ in Sec.V and $\Delta_x = \Delta_y \equiv \Delta$ in Secs.VI,VII.

To study the commensurability effects, the effective width of the channel is varied from a value $w/b_0 \sim 1-10$. We assume that the vortex density in and outside the channel are the same. The number of vortices in the channel is then given by $N_{ch} = (L/a_0)(w/b_0)$ with L the channel length. In a commensurate situation one has $w = pb_0$ and both the row spacing and (average) longitudinal vortex spacing in the channel match with the vortex configuration in the CE's. When $w \neq nb_0$ these spacings become different, leading to generation of topological defects. While this model differs from the experimental case where the applied field drives the incommensurability, the method offers a simple way of introducing geometrical frustration and study various (mis)matching configurations.

With a uniform transport current J applied perpendicular to the channel, the equation of motion for vortex i in the channel reads (in units of N/m):

$$\gamma \partial_t \mathbf{r}_i = f - \sum_{j \neq i} \nabla V(\mathbf{r}_i - \mathbf{r}_j) - \sum_{n,m} \nabla V(\mathbf{r}_i - \mathbf{R}_{n,m}). \quad (5)$$

$V(\mathbf{r})$ is the vortex-vortex interaction potential, j labels other vortices inside the channel, the damping parameter

γ is given by $\gamma = B\Phi_0/\rho_f$ with ρ_f the flux flow resistivity, and $f = J\Phi_0$ is the drive along the channel. For films which are not too thin compared to the penetration depth λ and magnetic fields small compared to the upper critical field B_{c2}, the interaction $V(\mathbf{r})$ is given by the London potential:

$$V(\mathbf{r}) = U_0 K_0(|\mathbf{r}|/\lambda), \qquad (6)$$

where $U_0 = \Phi_0^2/2\pi\mu_0\lambda^2$ and Φ_0 is the flux quantum.

In the simulations we integrate Eq.(5) numerically for all vortices in the channel. We use a Runge-Kutta method with variable time steps such that the maximum vortex displacement in one iteration was $a_0/50$. Distances were measured in units a_0 ($\bar{\mathbf{r}} = \mathbf{r}/a_0$), forces in units U_0/a_0 and time in units $\gamma a_0^2/U_0$. Following Ref. [37], the London potential was approximated by:

$$V(\bar{\mathbf{r}}) = \ln\left(\frac{r_c}{|\bar{\mathbf{r}}|}\right) + \left(\frac{|\bar{\mathbf{r}}|}{r_c}\right)^2 - \frac{1}{4}\left(\frac{|\bar{\mathbf{r}}|}{r_c}\right)^4 - 0.75, \qquad (7)$$

with a cut-off radius r_c corresponding to $r_c \simeq 3\lambda/a_0$. We performed most simulations for $r_c = 3.33$. Periodic boundary conditions in the channel direction were employed. For each w/b_0 we relaxed the system to the ground state for $f = 0$. We found that this is best achieved by starting from a uniformly stretched or compressed n or $n \pm 1$ configuration. For an initial configuration with N_{ch} vortices distributed randomly in the channel, relaxation resulted in (slightly) metastable structures, even when employing a finite temperature, simulated annealing method. Some peculiarities associated with such structures are mentioned in Secs.IV and VI. After the $f = 0$ relaxation, the average velocity versus force (v-f) curve was recorded by stepwise varying the force from large $f_{max} \to 0$ (occasionally $f = 0 \to f_{max} \to 0$ was used to check for hysteresis). At each force we measured $v(f) = \langle \dot{x}_i \rangle_{i,t}$ after the temporal variations in v became $< 0.5\%$ (ignoring transients by discarding the data within the first $3a_0$). In addition, at each force we measured several other quantities, e.g. the temporal evolution of $\mathbf{r_i}$ and the time dependent velocity $v(t) = \langle \dot{x}_i \rangle_i$.

III. SINGLE CHAIN IN AN ORDERED CHANNEL

The first relevant issue for plastic flow and commensurability effects in the channel is to understand the influence of periodically organized vortices in the CE's (see Fig. 3a). The characteristic differences between commensurate and incommensurate behavior can be well understood by focusing on a 1-D model in which only a single vortex chain is present in the channel. Therefore the CE's are assumed to be symmetric with respect to $y = 0$ (i.e. $\Delta x = 0$ in Fig. 3) and only the longitudinal degrees of freedom of the chain are retained. At commensurability, $w = b_0$, the longitudinal vortex spacing $a = a_0$. For

$w \neq b_0$ the average spacing $a = \Phi_0/(Bw) = a_0 b_0/w$ does not match with the period a_0 in the edges and interstitials or vacancies develop in the channel. Their density c_d is given by $c_d = |a_0^{-1} - a^{-1}| = (1/a_0)|1 - (w/b_0)|$.

A. Continuum sine-Gordon description

We first consider the interaction of a vortex in the channel with the periodic arrays in the CE's. As shown in App.A, when $B \lesssim 0.2B_{c2}$ and $\lambda \gtrsim a_0$ the edge potential arising from this interaction is:

$$V_{ce,0}(x,y) = -2U_0 e^{-k_0(w+b_0)/2}\cosh(k_0 y)\cos k_0 x, \quad (8)$$

where $k_0 = 2\pi/a_0$. For $w = b_0$ and $y = 0$, the associated sinusoidal force caused by the edge has an amplitude which we denote by μ:

$$\mu = (4\pi U_0/a_0)e^{-\pi\sqrt{3}} \simeq U_0/(6\pi a_0). \qquad (9)$$

Next we consider a static chain of vortices *inside* the channel. The chain is most easily described in terms of a continuous displacement field $u(x)$, representing the deviations of vortices in the chain with respect to the commensurate positions, i.e. $u(ia_0) = u_i = x_i - ia_0$. The edge force is then given as $f_p = -\mu\sin(k_0 u)$. To describe the interaction between vortices *within* the chain, we assume that their relative displacements are small, $\partial_x u \ll 1$. Then one can use linear elasticity theory. Taking into account that the interaction range $\lambda > a_0$, the elastic force at $x = ia_0$ is:

$$f_{el} = \sum_{s=ja_0 > ia_0} \partial_s^2 V(s)[u(x+s) + u(x-s) - 2u(x)]. \quad (10)$$

Using the Fourier transform of V the force due to a displacement $u_q(x) = \mathrm{Re}(u_q e^{iqx})$ with wave vector q is:

$$f_{el} = \int \frac{dk}{2\pi}\frac{U_0\pi k^2}{\sqrt{k^2 + \lambda^{-2}}}\sum_{s>x} 2e^{iks}[1 - \cos(qs)]u(x). \quad (11)$$

Recasting this into a sum over reciprocal vectors $lk_0 \pm q$ and retaining only the $l = 0$ term, one obtains the following dispersive elastic modulus of the chain:

$$\kappa_q = \frac{U_0\pi\lambda/a_0}{\sqrt{1 + \lambda^2 q^2}}. \qquad (12)$$

For deformations of scale $> 2\pi\lambda$, the elastic force is $f_{el} = \kappa_0\partial_x^2 u$ with a long wavelength stiffness $\kappa_0 = U_0\pi(\lambda/a_0)$.

The equation of motion for u for a uniformly driven chain, is obtained by adding the driving force f to the edge force and the intra-chain interactions resulting in: $\gamma\partial_t u = f + f_p + f_{el}$. Assuming for the moment that the long wavelength description is valid, the evolution of u is given by the following sine Gordon (s-G) equation:

$$\gamma\partial_t u = f - \mu\sin(k_0 u) + \kappa_0\partial_x^2 u \qquad (13)$$
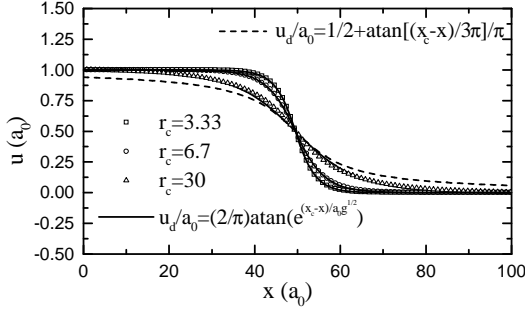
FIG. 4: Drawn lines: the anti-kink solution Eq.(14) for $\lambda/a_0 = 1$, 2 and 9 (most extended line). Symbols: numerically obtained displacement field for an isolated interstitial for the corresponding r_c. Dashed line: defect shape Eq.(18) in the nonlocal limit.

A useful visual representation of Eq.(13) is an elastic string of stiffness κ_0 with transverse coordinate $u(x)$ in a tilted washboard potential $(\mu/k_0)\cos(k_0 u) - fu$.

The s-G equation (13) has been thoroughly studied in different contexts (e.g. [38, 39, 40]). In the static case ($f = 0$), it has the trivial solution $u = 0$, corresponding to a commensurate chain, or kinked, incommensurate, solutions in which $u(x)$ periodically jumps by $\pm a_0$, each jump representing a point defect in the channel. In the context of long Josephson junctions (LJJs, [38]), a kink corresponds to a Josephson vortex where the phase difference across the junction changes by 2π. An *isolated* defect is represented by the familiar 'soliton' solution of the s-G model:

$$u_d(x) = 2a_0 \arctan[\exp(\pm 2\pi(x - x_c)/l_d)]/\pi. \quad (14)$$

Here x_c denotes the center of the defect and the $+$ $(-)$ sign denotes a vacancy or interstitial (kink or antikink). The length l_d represent the core size of the defect:

$$l_d = 2\pi a_0 \sqrt{g}, \quad (15)$$

with g the dimensionless ratio between the chain stiffness and maximum curvature of the pinning potential:

$$g = \kappa_0/2\pi\mu a_0 = 3\pi(\lambda/a_0), \quad (16)$$

as follows from Eq.(9),(12). For $\lambda/a_0 \gtrsim 1$, l_d thus considerably exceeds the lattice spacing. The continuum approach is validated since $\partial_x u_d \lesssim 2a_0/l_d \ll 1$. In Fig. 4 we have illustrated the characteristic defect shape Eq.(14), along with numerical data from a later section.

The long wavelength limit is only valid when l_d considerably exceeds λ. Since l_d grows only as $\sqrt{\lambda/a_0}$ the dispersion in the elastic interactions becomes important beyond a certain value of λ/a_0. This value is estimated by setting $\lambda q_d = 2\pi\lambda/l_d = 1$ in Eq.(12), resulting in $\lambda/a_0 \simeq 9$, in which case $l_d \simeq 54a_0$.

For larger interaction range one employs the following approach, first derived by Gurevich [28] for mixed Abrikosov-Josephson vortices in grain boundaries. Expression (10) for the elastic force can be written as an integral $f_{el} = \int (ds/a_0)\partial_s^2 V(s)u(x + s)$. For defects on a scale $< \lambda$, only the short distance behavior of V has to be retained: $V(x) = U_0 K_0(x/\lambda) \approx -U_0 \ln(|x/\lambda|)$. Integrating the expression for f_{el} by parts and adding the edge force and the drive, the equation of motion becomes:

$$\gamma\partial_t u = f - \mu\sin(k_0 u) + (U_0/a_0)\int_{-\infty}^{\infty} ds \frac{\partial_s u}{s - x}. \quad (17)$$

A static solution of Eq.(17) for a single defect is [28]:

$$k_0 u = \pi + \arctan(\pm 2\pi x/l_d^{nl}), \quad (18)$$

with $l_d^{nl} = 6\pi^2 a_0$, which is valid when $\lambda > l_d^{nl}$. The value for l_d^{nl} is nearly the same as the s-G core size l_d for $\lambda/a_0 = 9$. This means that upon approaching the nonlocal regime, the increase of core size saturates at $\sim 60a_0$, while only the tails of the defect are affected according to Eq.(18), see Fig. 4. A more accurate calculation of the onset of the nonlocal field regime using Brandt's field-dependent vortex interaction (App.A) shows that non-locality is only relevant for a channel in a superconductor with $\lambda/\xi \gtrsim 50$.

So far, we discussed isolated defects. For finite defect density, the repulsive interaction between defects of the same 'sign' causes a periodic superstructure in the chain. When c_d grows to $\sim 1/l_d$, the defects start to overlap significantly. For the (local) s-G model, explicit solutions for u have been obtained in terms of the Jacobi elliptic functions, for which we refer to [38, 40]. Recently, also in the non-local limit where $l_d^{nl} > \lambda$, the 'soliton' chain has been described analytically [28], which we will not repeat here.

B. Transport properties

With a uniform drive f, the transport properties strongly depend on the presence and density of defects in the channel. At commensurability ($a = a_0$, $c_d = 0$), a threshold force $f_s = \mu$ is required, above which all vortices start moving uniformly. Their velocity is identical to that of an overdamped particle in a sinusoidal potential: $v = \sqrt{f^2 - \mu^2}$ [41]. The threshold μ coincides with the well known relation between shear strength and shear modulus of an ideal lattice by Frenkel [36]: for a harmonic shear interaction, a value $A = A^0 = a_0/(2\pi b_0) = 1/\pi\sqrt{3}$ applies in Eq.(1). Identifying $F_s a_0 b_0 = f_s = \mu$ for $w = b_0$, one finds:

$$c_{66} = \pi\sqrt{3}\mu/(2a_0) = U_0/(8a_0 b_0), \quad (19)$$

which coincides with the familiar expression for the shear modulus in the London limit: $c_{66} = \Phi_0 B/(16\pi\mu_0\lambda^2)$. In App.A we generalize the expression for the ordered channel potential to higher field and show that also in that case the potential is harmonic and that $A = A^0$ holds for a commensurate channel.

At incommensurability, depinning of the chain is governed by the threshold force to move a defect. In

the present continuum approach such threshold is absent. However, taking into account the discreteness of the chain, in which case Eq.(13) turns into a Frenkel-Kontorova (FK) model [35], a finite Peierls-Nabarro (PN) barrier exists to move a defect over one lattice spacing (see e.g. [40]). The magnitude of the PN barrier has been studied for a variety of cases, including FK-models with anharmonic and/or long-range interactions [40, 42]. For $g < 1$, f_{PN} can amount to a considerable fraction of μ. Additionally, in this regime anharmonicity may renormalize g [40, 42] and cause pronounced differences between the properties of kinks (vacancies) and antikinks (interstitials). In our limit $g \gg 1$, where $\partial_x u \ll 1$ and harmonic elastic theory applies, these differences are small and the pinning force vanishes as $f_{PN} = 32\pi^2 g\mu \exp\left(-\pi^2\sqrt{g}\right)$. Hence, defects in an ordered channel give rise to an essentially vanishing plastic depinning current J_s [43].

Considering the dynamics, for small drive $f < \mu$ the motion of defects, each carrying a flux quantum, provides the flux transport through the channel. When defects are well separated, for $c_d < l_d^{-1}$, the mobility of the chain is drastically reduced compared to free flux flow and the average velocity v is proportional to the defect density: $v = c_d v_d a_0$. Here v_d is the velocity of an isolated defect at small drive. It can be calculated from the general requirement that the input power must equal the average dissipation rate:

$$f v = \gamma \langle (\partial_t u)^2 \rangle_{L,t} = (\gamma/l_d) \int^{l_d} (\partial_t u)^2 dx. \qquad (20)$$

The last step arises from the space and time periodicity of u. Using $\partial_t u = v_d \partial_x u$ and the kinkshape Eq.(14), one obtains the 'flux flow resistivity' at small defect density:

$$dv/df = c_d a_0 (\pi^2 \sqrt{g}/2\gamma), \qquad (21)$$

where $\pi^2 \sqrt{g}/2\gamma = M_d$ is the kink mobility in the s-G model [39]. For larger defect density, where defects start to overlap this relation changes. The linear response for $f \lesssim \mu$ may then be obtained from the solutions for u based on elliptic integrals [28, 38, 40].

For larger drive $f \gtrsim \mu$, the 'tilt' induced reduction of the (washboard) edge potential becomes important. This leads to an expansion of the cores of the sliding defects and causes a nonlinear upturn in the v-f curves. Exact solutions of Eq.13 describing this behavior do not exist. Therefore we use a perturbative method similar to that in [22, 44] which is able to describe the full v-f curve over a wide range of defect densities. It is convenient to define the displacements $h(x, t) = u(x, t) - s(x, t)$, where $s(x, t) = (q/k_0)x + vt$, with $(q/k_0) = c_d a_0$, is the continuous field describing the displacements of an undeformed incommensurate chain (i.e. straight misoriented string in the washboard potential) moving with velocity v. In terms of h, the equation of motion (13) and Eq.(20) can be written as:

$$\gamma v(1 + \partial_s h) = f + \mu \sin(k_0 h + qx + k_0 vt) + \kappa (q/k_0)^2 \partial_s^2 h \qquad (22)$$

$$f = \gamma v + (\gamma v/a_0) \int^{a_0} (\partial_s h)^2 ds. \qquad (23)$$

The last term in Eq.(23) describes additional dissipation due to internal degrees of freedom in the chain. Under influence of the potential, h acquires modulations with period $1/c_d$ in x, i.e. period a_0 in s. These modulations are then expressed as a Fourier series of modes with wavelength $1/(mc_d)$ (m integer ≥ 1) and amplitude h_m:

$$h(x, t) = \sum_m h_m \exp[imk_0 s] + c.c. \qquad (24)$$

The overlap of defects and the core expansion for $f \geq \mu$ appears in the q and v dependence of h. Both effects cause a reduction of the relative displacements h. An approximate solution for $h(v)$ is obtained by substituting Eq.(24) into Eq.(13), yielding the coefficients h_m (details of the solution are deferred to App.B). The v-f relation Eq.(23) attains the form:

$$f = \gamma v \left[1 + \frac{\omega_p^2}{2[\omega_0^2 + \omega_r^2]} \right]. \qquad (25)$$

The additional 'friction' force is represented in terms of the pinning frequency $\omega_p = \mu k_0/\gamma$, the washboard frequency $\omega_0 = k_0 v$ and $\omega_r = K_{eff}^2(c_d)/\gamma$ which is the effective relaxation frequency for nonlinear deformations associated with a defect density $c_d = q/(2\pi)$, with $K_{eff}^2(c_d)$ given in App.B. At small v, the elastic relaxation time $1/\omega_r$ for the chain to relax is much smaller than the timescale $1/\omega_0$ between passage of maxima in the edge potential. This corresponds to the linear sliding response of the static structure of (overlapping) defects. For large v, $1/\omega_r \gg 1/\omega_0$ meaning that the incommensurate chain is not given enough time to deform. This leads to expanded defects described by a sinusoidal variation of h with reduced amplitude (see App.B). The v-f curve then approaches free flux flow according to $f - \gamma v \sim v^{-1}$ as for a single particle.

Recently, exact solutions describing the nonlinear dynamics and core expansion of mixed Abrikosov-Josephson vortices based on the nonlocal Eq.(17) have been derived in [28]. The resulting transport curves are very similar to those obtained from Eq.(25), see Fig. 5. We also note the similarity with the IV curves obtained from a model for kinked Josepson strings [45] in high T_c superconductors with the field under an angle with respect to the insulating layers.

C. Numerical results

The simulations of symmetric channels ($\Delta x = 0$) for $w \sim b_0$ fully support the above findings. The interaction with the CE's for $w = b_0$ provides a maximum restoring force with a value 0.054, independent of the interaction cut-off r_c used in the numerics. This value is in agreement
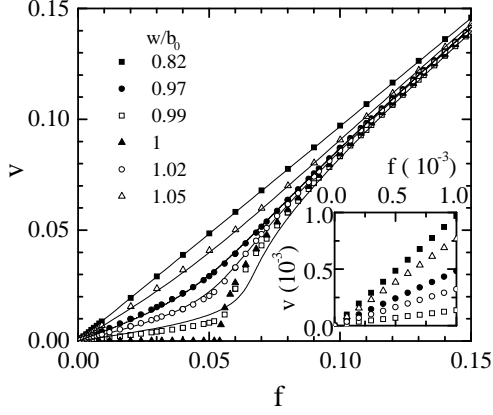
FIG. 5: v-f characteristics for ordered vortex channels with $w \approx b_0$ and $\Delta x = 0$. Symbols are simulation results, drawn lines are obtained with Eq.(25). The inset shows an expanded view of the small velocity regime.

with the dimensionless values for μ and c_{66} in Eq.(9) and (19): $a_0\mu/U_0 = 1/(6\pi)$ and $c_{66}a_0^2/U_0 = 1/(4\sqrt{3})$).

The data points in Fig. 4 show the displacement field of a single defect (obtained by adding one vortex to a commensurate chain) for three values of the cut-off r_c (i.e. various λ/a_0). We conclude that up to $r_c = 30$ ($\lambda/a_0 = 9$) the s-G kink shape Eq.(14) forms a good description of a defect in the chain.

The data points in Fig. 5 show numerical results for the transport of a single chain in channels of various widths and $r_c = 3.33$. The features discussed previously, i.e. the vanishing PN barrier and nonlinear transport, clearly appear in the data for incommensurate chains. We also plotted the results according to Eq.(25), with $K_{eff}^2(c_d)$ evaluated using the results in App.B for $\lambda/a_0 = 1$ and taking into account that μ slightly depends on w. The analytical treatment gives a very reasonable description of the data. Finally, we show in Fig. 6 the numerical results and analytical results of App.B for the quasi-static and dynamic shape of the chain for $w/b_0 = 0.97$ ($c_d = 0.03/a_0$). The numerical results closely mimic the analytic results, both for the kinked shape at small v and the core expansion with the associated reduction of h for large v.

To conclude this section we mention that, at incommensurability, due to the vanishing barrier for defect motion, the average velocity $\langle \dot{x}_i(t) \rangle_i$ has a vanishing ac-component. Only at commensurability the washboard modulation is retained, the velocity at large drive being $\langle v(t) \rangle = v + (\mu/\gamma)\sin(\omega_0 t)$.

IV. ORDERED CE'S AND MULTIPLE CHAINS

We now turn to the results for channels containing multiple vortex rows and ordered CE's. The simulations are performed with the full 2D degrees of freedom and
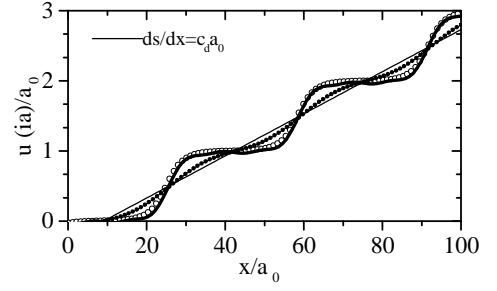

FIG. 6: Displacements $u(x)$ along the channel for $w = 0.97b_0$:($\circ$) Numerical result for $f = 0$ also representing a snapshot of the moving chain at low drive, $f = 0.01$. The thick drawn line shows the result for u as calculated from the Fourier modes given in App.B. ($\bullet$) Displacement field for $v = 0.09$ ($f = 0.1$). The data mask a drawn line which is obtained from Eq.(B8) in App.B. The straight drawn line shows the displacement field $s(x)$ in absence of the periodic potential.
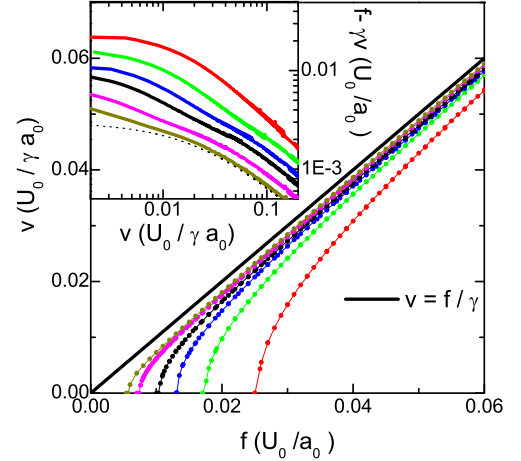

FIG. 7: Transport curves for commensurate channels with $w/b_0 = 2, 3, 4, 5, 7, 9$ from right to left. The thick drawn line represent free flux flow. Inset: friction force $f - \gamma v$ vs. v for $w/b_0 = 2, 3, 4, 5, 7, 9$ from top to bottom. The dotted line represents Eq.(28) for $n = 9$.

$r_c = 3.33$. We implemented an edge shift $\Delta x(w)$ with a saw tooth shape ($0 \le \Delta x \le a_0/2$). This assures that, as we vary w, a perfect hexagonal structure is retained for $w = pb_0$ with p an integer. However, for $w \ne pb_0$, the qualitative behavior did not depend on Δx.

Figure 7 shows v-f curves of commensurate channels, $w/b_0 = n$ with integer $n \ge 2$. In these cases the arrays are perfectly crystalline and have a shear strength $f_s = \mu b_0/w$, inversely proportional to the channel width and in accord with Eq.(1) with $A = A^0 = 1/\pi\sqrt{3}$. This is consistent with the fact that only the first mobile chains within a distance $\sim b_0$ from both CE's experience the periodic edge potential (see Eq.(A3)) while the other chains provide an additional pulling force via the elastic interaction. This interaction brings an additional feature to the dynamics, namely shear waves. The shear displacements

of rows n in the bulk of the channel can be described in continuum form, $u_n(t) \rightarrow u(y,t)$, by the following equation of motion:

$$\gamma \partial_t u(y,t) = f + c_{66} a_0 b_0 \partial_y^2 u(y,t). \qquad (26)$$

At large v the CE interaction can be represented by oscillating boundary conditions. As shown in App.C, this causes an oscillatory velocity component dh/dt with y-dependent amplitude and phase describing periodic lagging or advancing of chains with respect to each other:

$$\partial_t h(y,t) \sim -f(y)\sin(\omega_0 t) - g(y)\cos(\omega_0 t). \qquad (27)$$

Here ω_0 is the washboard frequency $k_0 v$, $f(y) = \cos(y/l_{\perp,v})\cosh(y/l_{\perp,v})$, $g(y) = \sin(y/l_{\perp,v})\sinh(y/l_{\perp,v})$. The length scale $l_{\perp,v} = \sqrt{(\mu/\gamma v)}b_0$ explicitly depends on v and represents the distance over which the amplitude and phase difference decay away from the CE's. Although in principle Eq.(27) is only valid for $\gamma v/\mu \gtrsim 0.25$, it provides useful qualitative insight in the dynamics at all velocities: at small velocity $l_{\perp,v}$ is large, meaning that for all rows the velocity modulation and phase become similar. Hence, for $v \rightarrow 0$ the array may be described as a single vortex chain, which is the underlying origin of the fact that close to threshold the curves approach the 1D commensurate behavior $v = \sqrt{f^2 - f_s^2}$ with reduced threshold $f_s = \mu/n$. At large velocity, $l_{\perp,v}$ eventually becomes less than the row spacing. In that limit only the two chains closest to the CE experience a significant modulation. In App.C we quantitatively analyze the friction force in this regime with the result:

$$f - \gamma v = \frac{\mu^2}{2n(2\gamma v + \mu)}. \qquad (28)$$

In the inset of Fig. 7 this behavior is displayed for $n = 9$ by the dotted line. In the high velocity regime the result agrees well with the numerical data, at lower velocities Eq.(28) underestimates the true friction.

Next we discuss the behavior of incommensurate channels. The static vortex configuration for a channel of width $w/b_0 = 3.92$ is shown in the upper part of Fig. 8. A Delauney triangulation shows that the array consists of 4 rows with two pairs of 5,7-fold coordinated vortices at the CE constituting two misfit dislocations of opposite Burgers vector $\vec{b}$ and glide planes along x. Due to their mutual attraction, dislocations at the upper and lower CE are situated along a line with an angle of $\sim 60°$ with $\vec{x}$. The two edge dislocations thus form a 'transverse' stacking fault (TSF). In the lower part of Fig. 8 the structure for a channel with $w/b_0 = 3.52$ is shown. Here the density of stacks, given by $c_{TSF} = |(1/a_0) - (1/a)|$, is enhanced. The dislocations at one side of the CE repel each other and are equally spaced, like the periodic superstructure for a single chain in Fig. 6. The slight misalignment between the 'upper' and 'lower' dislocations of a pair is due to the relative shift between the CE's: the exact orientation of the pairs is determined
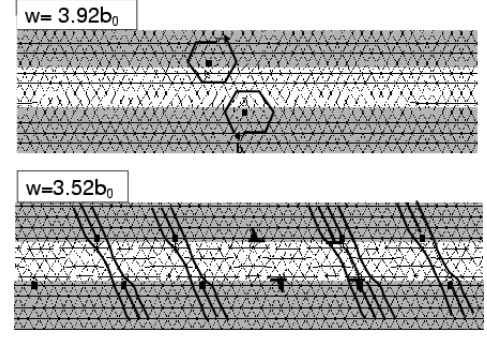

FIG. 8: Delauney triangulation of the static structure for two incommensurate channels: $w/b_0 = 3.92$ and $w/b_0 = 3.52$. Open circles and filled squares denote 7 and 5-fold coordinated points, respectively. The construction for the Burgers vector is shown for $w/b_0 = 3.92$; the drawn lines for $w/b_0 = 3.52$ mark the transverse stacking faults.
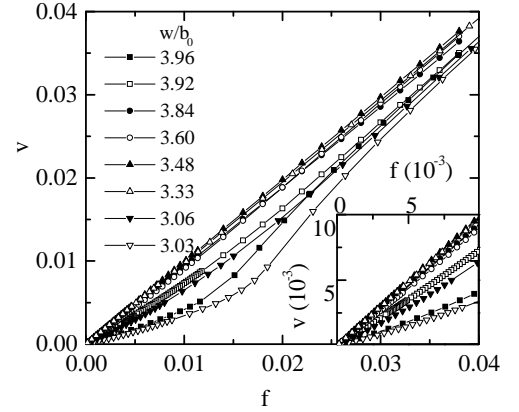

FIG. 9: v-f curves for incommensurate channels. Inset: regime of small drive.

by the choice of Δx. For channel widths in the regime $n < w/b_0 \lesssim n + 1/2$ with integer n, we find very similar structures but instead of TSF's consisting of vacancies, we now have TSF's consisting of *interstitial vortices*, again arranged in a periodic superstructure.

Figure 9 shows the transport curves associated with these structures. As for the single chain, the presence of misfit defects causes an essentially vanishing threshold force. For small drive, $f < \mu b_0/w$, a low mobility regime occurs associated with glide of the edge dislocation pairs along the CE. This allows for elastic motion of a complete TSF, i.e. the vortices in the 'bulk' of the channel remain 6-fold coordinated.

It is interesting to study how the mobility due to the TSF's changes on increasing the number of rows. In Fig. 10 we plot the mobility per stack, $M_{TSF} = (dv/df)_{f \rightarrow 0}/c_{TSF}$ versus channel width. M_{TSF} around each peak decreases with increasing c_{TSF}. This is caused by overlap of the strain fields of the defects, in analogy with the behavior for a single chain. The overall increase of the peak value of M_{TSF} is related to a change in the
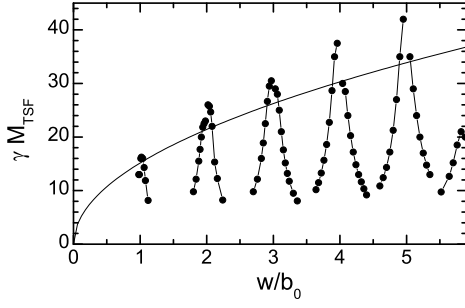
FIG. 10: The mobility per stack $M_{TSF} = (dv/df)/c_{stack}$ versus w/b_0. The drawn line shows the predicted form Eq.(29) for $\lambda/a_0 = 1$.
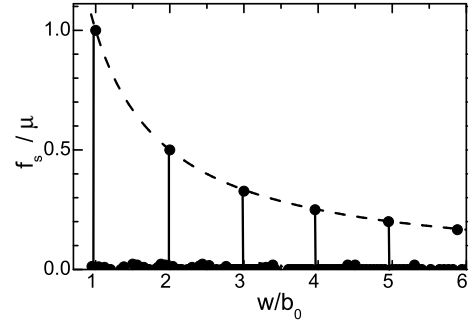

FIG. 11: Threshold force versus w/b_0 for ordered channels. The dashed line represents Frenkels prediction for an ideal lattice in the continuum limit.

size of an isolated TSF. An extension of the analysis in Sec.III allows to describe this change quantitatively. For small n the longitudinal deformations do not vary strongly over the channel width. This can be understood by considering shear and compression deformations related by the equation $\kappa \partial_x^2 u_x + c_{66} a_0 b_0 \partial_y^2 u_x = 0$. It follows that a longitudinal deformation on a scale $l_\parallel$ along the channel varies over a scale $l_\perp = l_\parallel \sqrt{c_{66} a_0 b_0/\kappa}$ perpendicular to the channel. In case $l_\perp \gtrsim w$, the transverse variation of $u_x(y)$ is small and can be neglected so that κ_0 in Eq.(13) can be replaced by an effective stiffness $n\kappa_0$ due to n rows. Similarly, the driving force is replaced by $f \to nf$. This results in the same equation (13) with a rescaled edge force $\mu \to \mu/n$. Accordingly, the longitudinal size of a defect (TSF) is given by $l_{TSF} = 2\pi a_0 \sqrt{ng}$ and the mobility of an isolated TSF by (compare M_d below Eq.(21)):

$$M_{TSF} \simeq \pi^2 \sqrt{ng}/2\gamma. \qquad (29)$$

As shown by the drawn line in Fig. 10, this form gives a reasonable description of the data up to $n = 3$. Working out the condition $l_\perp \gtrsim w$ given above for the validity of Eq.(29), one obtains $w \lesssim (l_d/2)\sqrt{c_{66} a_0 b_0/\kappa} \simeq 3b_0$, in agreement with the data. At larger n, 'bulk-mediated' elasticity [46] leads to decay of the longitudinal deformations towards the channel center. We also note that, due to the increase of l_{TSF} with n, the density c_{TSF} for which defects are non-overlapping, decreases on increasing n.

In the v-f curves of Fig. 9 we observe at larger velocity features very similar to the transport of the 1D chain: for $f \gtrsim \mu/n$ the effective barrier is reduced, leading to core expansion of the TSF's. Accordingly, the curves approach free flux flow behavior. As in the commensurate case, this approach is initially more slowly then $f - \gamma v \sim 1/v$ due to additional oscillating shear deformations in the channel for $f \gtrsim \mu/n$.

Figure 11 summarizes the behavior of the shear force f_s, taken at a velocity criterion $v \approx 0.01\mu/\gamma$, versus the matching parameter. At integer $w/b_0 = n$, the threshold is $f_s = \mu/n$, but we note that it can be reduced due to a finite edge shift Δx. At mismatch f_s is essentially vanishing. Near 'half filling', $w/b_0 \simeq n \pm 1/2$, where the arrays

switch from n to $n\pm 1$ chains, a small enhancement of f_s is observed. In this regime, the static ($f = 0$) structure was obtained by annealing from a random initial configuration, attempting to determine the exact switching point. This results in metastable structures with coexisting n and $n \pm 1$ row regions (or longitudinal stacking faults, LSF's) bordered by dislocations with misoriented Burgers vector, see [35]. The increase in f_s is caused by the finite barrier for climb-like motion of these dislocations, via which an LSF can move as 'giant' defect through the channel. For sufficiently large drive, (part of) the LSF's are annealed which may result in hysteresis for up/down cycled v-f curves. We will discuss these 'mixed' $n/n \pm 1$ structures in more detail in Secs.VI and VII in the context of disordered CE's. We also note that the integer chain structures with TSF's away from half filling differ from the results in [35]. The structures there, obtained from a random initial configuration, contained point defects unequally distributed among rows, yielding 'gliding' dislocations within the channel. Such structures are also slightly metastable but the conclusion of vanishing f_s for incommensurate, integer chain structures, drawn in [35], remains unaltered.

V. SINGLE CHAIN IN A DISORDERED CHANNEL

We will now consider the influence of disorder in the CE arrays on transport in the channels, focussing in this section on the characteristics of a single chain for $w/b_0 \sim 1$ with only longitudinal degrees of freedom. The CE disorder is implemented with longitudinal random shifts as described in Sec.II. We note that both CE's remain 'in phase'; the effect of quenched phase slips or dislocations between the CE's will be treated in the discussion in Sec.VIII.

A. Disordered sine-Gordon equation

First we consider the form of the channel potential in presence of weak disorder. To that end we generalize Eq.(A1) in App.A and express the CE potential at $\mathbf{r_0} = (x, y = 0)$ in terms of the vortex density ρ_e in the CE's:

$$V_{ce}(\mathbf{r_0}) = (2\pi)^{-2} \int d\mathbf{k} V(\mathbf{k}) \rho_e(\mathbf{k}) e^{i\mathbf{k} \cdot \mathbf{r_0}}, \qquad (30)$$

with $\rho_e(\mathbf{k})$ the Fourier transform of ρ_e. For weak disorder ($\nabla \cdot \mathbf{d} \ll 1$), this density can be expressed in terms of the displacement field $\mathbf{d}$ in the CE as follows [47]: $\rho_e(\mathbf{r}_e, \mathbf{d}) \simeq (B/\Phi_0)(1 - \nabla \cdot \mathbf{d} + \delta\rho_e)$ where $\delta\rho_e = \sum_i \cos[\mathbf{K}_i(\mathbf{r}_e - \mathbf{d}(\mathbf{r}_e))]$ represents the microscopic modulation due to the lattice ($\mathbf{K}_i$ spans the reciprocal lattice) while $\nabla \cdot \mathbf{d}$ reflects density modulations. As described in App.D, this decomposition of ρ_e leads to two contributions to the potential:

$$\begin{aligned} V_{ce} = \quad & V_l(x) + V_p(x) \\ = \quad & -(B/\Phi_0) \int d\mathbf{r}_e V(\mathbf{r_0} - \mathbf{r}_e) \nabla \cdot \mathbf{d}(\mathbf{r}_e) \\ & -[\mu + \delta\mu(x)] \cos[k_0(x - d)]/k_0, \qquad (31) \end{aligned}$$

where in the second term $\delta\mu(x)/\mu = \pi\sqrt{3}\partial_x d$. The term V_l represents long range potential fluctuations and is smooth on the scale $\sim a_0$. Its correlator $\Gamma_l(s) = \langle V_l(x) V_l(x + s) \rangle$ is derived in App.D. Assuming that $\partial_x d$ has short range correlations (on the scale $\sim a_0/2$) and a variance $\langle (\partial_x d)^2 \rangle = \Delta^2/3$ as in the simulations, Γ_l can be written as:

$$\Gamma_l(s) \simeq C_\alpha \Delta^2 U_0^2 (\lambda/a_0)^{1+\alpha} e^{-(\frac{s}{\lambda})^2}. \qquad (32)$$

The exponent α and the prefactor C_α depend on the disorder correlations between rows in the edge: $\alpha = 2$ when the strain $\partial_x d(x)$ is identical for all rows and $\alpha = 1$ when the strain is uncorrelated between rows. The term V_p in Eq.(31) is the quasi-periodic potential arising from $\delta\rho_e$ of the vortex rows nearest to the CE's. The amplitude fluctuations $\delta\mu/k_0$ are characterized by (see App.D):

$$\Gamma_a(s) = \frac{\langle \delta\mu(x)\delta\mu(x + s) \rangle_x}{k_0^2} \simeq (\mu\Delta a_0/2)^2 e^{-(\frac{2s}{a_0})^2} \qquad (33)$$

To obtain the energy of the vortex chain and the equation of motion, the vortex density inside the channel, ρ_c, is decomposed similar to ρ_e: $\rho_c(x, u) = a_0^{-1}[1 - \partial_x u + \delta\rho_c(x, u)]$, where u is the displacement field of the chain. As shown in App.D, in the limit $\lambda > a_0$ the resulting interaction with the CE's can be written as $H = H_{SG} + H_a + H_s$ where $H_{SG} = a_0^{-1} \int dx[(\kappa_0/2)(\partial_x u)^2 - (\mu/k_0)\cos(k_0 u)]$ represents the sine-Gordon functional for an ordered channel, and H_a, H_s are the disorder contributions due to amplitude fluctuations and random coupling to the strain:

$$\begin{aligned} H_a = & -\int \frac{dx}{a_0} \frac{\delta\mu(x)}{k_0} \cos(k_0 u) \\ H_s = & -\int \frac{dx}{a_0} V_s(x) \partial_x u. \qquad (34) \end{aligned}$$

The term $V_s(x) = V_l(x) - \kappa_0\partial_x d(x)$ contains contributions from local and nonlocal strains. The latter dominates for $\lambda > a_0$ (see App.D). Hence $\Gamma_s(s) = \langle V_s(x)V_s(x + s) \rangle \simeq \Gamma_l(s)$.

The model described by $H = H_{SG} + H_a + H_s$ is also used to describe LJJs or commensurate CDW's with weak disorder, however with different disorder correlations. In the former case, the term H_a in Eq.(34) describes local variations in the junctions critical current [48, 49]. For CDW's, a disorder contribution of the form H_a arises from so called backward scattering impurities, while the term H_s originates from 'forward' scattering impurities [50]. We also note that our model differs from the usual Fukuyama-Lee-Rice model for CDW's [51], in which commensurability is ignored either due to strong direct random coupling to u ($\delta\mu(x) \gg \mu$) or due to large mismatch.

In principle, the equation of motion for the chain is given by $\gamma\partial_t u = -\delta H/\delta u$. However, it has been shown in previous studies [46, 52, 53, 54] that in the moving state a convective term $-\gamma v \partial_x u$ should be included. While irrelevant for the depinning process, such term can be important for the dynamics and for completeness we include it [55]. The resulting equation of motion is:

$$\begin{aligned} \gamma\partial_t u = \quad & f + \kappa_0\partial_x^2 u - [\mu + \delta\mu(x)]\sin(k_0 u) \\ & -\partial_x V_s - \gamma v \partial_x u. \qquad (35) \end{aligned}$$

In writing Eq.(35) we have assumed, for simplicity, that the elastic deformations in presence of disorder can be described by the long wavelength stiffness κ_0. Ignoring the last term, Eq.(35) describes the transverse displacements $u(x)$ of an elastic string in a tilted 'washboard' potential with random amplitude $\mu(x)/k_0$ and random phase $\phi(x) = -\int_{-\infty}^{x} dx' V_s(x')/\kappa_0$. The latter represents a u independent random deformation of the chain.

B. Numerical results

The influence of disorder on the threshold force and the dynamics of the chain are directly visible in numerical simulations. The simulations were performed using $r_c = 3.33a_0$ and channels of length $L \geq 1000a_0$.

Figure 12 shows several v-f curves for channels with $0.93 < w/b_0 < 1.1$ at a disorder strength $\Delta = 0.025$. We first focus on the result for the commensurate case $w = b_0$. The disorder leads to a significant reduction of the threshold f_s with respect to the pure value $\mu = 0.054$. The reduction is enhanced on increasing Δ, as shown for $\Delta = 0.05$ in the inset. The origin of the reduction
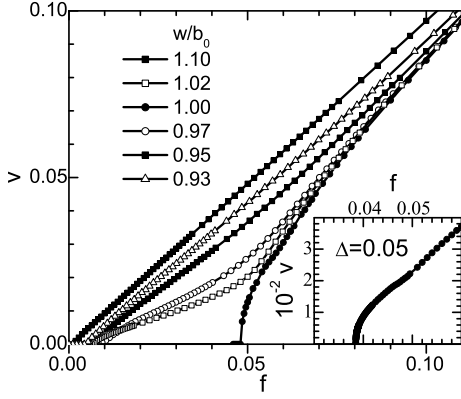
FIG. 12: *v-f* curves of a commensurate and various incommensurate chains for weak disorder $\Delta = 0.025$. Inset: *v-f* curve of a commensurate channel for $\Delta = 0.05$

is that disorder lowers the energy barrier for formation of vacancy/interstitial (kink/antikink) pairs in the chain. Figure 13a shows the time evolution of the displacements $u_i = x_i - ia_0$ upon a sudden increase of f to a value $f = 0.049 > f_s$ at t_1. For $t < t_1$ u is 'flat' and the 2D crystal formed by the chain and the CE's is topologically ordered. At $t = t_1$, the motion starts at an unstable site (at $x/a_0 \simeq 500$) by nucleation of a vacancy/interstitial pair visible as steps of $\pm a_0$ in u. We henceforth denote the force at which this local nucleation occurs by f_n. The defects are driven apart by the applied force and when their spacing becomes $\sim l_d$ a new pair nucleates at the same site. This process occurs periodically with rate R_n, leading to the formation of a domain with defect density $c_d = R_n/\langle v_d \rangle$ and a net velocity $v = c_d \langle v_d \rangle a_0 = R_n a_0$ with $\langle v_d \rangle$ the average defect velocity. In the present case of weak disorder $\langle v_d \rangle$ is essentially the same as for $\Delta = 0$. For a further increase of the force to $f = 0.053$ an increase of the nucleation rate is observed. In Ref.[33] we showed that in larger systems coarsening occurs in the initial stage of depinning due to a distribution of unstable sites. However, after sufficiently long times the stationary state consists of one domain around the site with the largest nucleation rate (smallest local threshold f_n^{min}) with vacancies travelling to the left and interstitials to the right. It is interesting to compare this to a study of CDW's with competing disorder and commensurability pinning [52]. Using a coarse grained version of Eq.(35) it was found in [52] that in the pinning dominated, low velocity regime, the so-called interface width $W(L) = \sqrt{\langle (u(x) - \langle u \rangle)^2 \rangle_x}$ grows linearly with the system size L. The mechanism of defect nucleation which we observe naturally explains this phenomenon. In addition, we found that at depinning the average velocity $v = R_n^{max} a_0$ can be described by $R_n^{max} \propto (f - f_n^{min})^\beta$ with a depinning exponent $\beta = 0.46 \pm 0.04$, similar as previously reported for 1D periodic media [56].

The defective flow profile does not persist up to a arbitrary large forces. In the commensurate *v-f* curve in Fig. 12 and its inset, a small kink is observed for $f \lesssim \mu$. Asso-
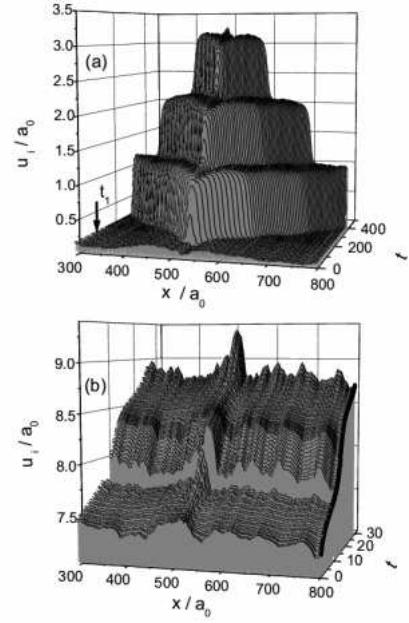

FIG. 13: (a) Evolution of *longitudinal* displacements $u_i(t)$ for the commensurate chain in Fig. 12($\Delta = 0.025$), plotted for clarity in a transverse way vs. x. At $t = t_1$ the force is increased above threshold. (b) Stationary evolution of $u_i(t)$ for large drive ($f = 0.08$) showing the motion over a distance $\sim 1.8a_0$ (the t and u axis have arbitrary offset, and a few frames around $t = 10$ were omitted for clarity).

ciated with this kink we find a transition to a much more ordered state. We have illustrated the temporal evolution of vortex displacements in this state in Fig. 13(b) for $f = 0.08$. The 'staircase' structure has vanished and the relative vortex displacements are greatly reduced. In fact, in the above mentioned study Ref. [52] a very similar transition in the CDW dynamics was found, and was shown to be of first order. We leave the precise dependence of this transition on disorder and vortex interactions in our channels for future studies.

We now turn to the incommensurate case. The *v-f* curves with $w \neq b_0$ in Fig. 12 all exhibit a finite threshold instead of the vanishing threshold for the incommensurate channels without disorder (Fig. 5). With disorder the defects that are present in the channel, couple to the disorder in the CE, which causes a pinning barrier f_d. This barrier has a distribution along the channel $\{f_d\}$ and maximum value f_d^{max}. We now focus on the curves with small defect density $c_d \lesssim 1/l_d$ for which the defects are individually pinned. In this regime the threshold force f_s satisfies $f_s \lesssim f_d^{max}$.

The precise threshold behavior depends on the distribution of barriers $\{f_d\}$, similar as for LJJ and CDW systems [48]. As an illustration, we show in Fig. 14(a) the evolution of displacements for a channel with $w/b_0 = 0.99$ for a force just above threshold $f(t > 0) > f_s$. The static configuration at $t = 0$ ($f < f_s$) shows that the disorder breaks the periodicity of the 'soliton' chain. For $t > 0$, de-

FIG. 15: Threshold f_s, obtained from a velocity criterion $v \approx 0.025\mu/\gamma$ and $L = 1000a_0$, versus w/b_0 for several disorder strengths. Data were averaged over 5 disorder realizations. Inset: v-f curves in the strong disorder regime $\Delta = 0.2$.
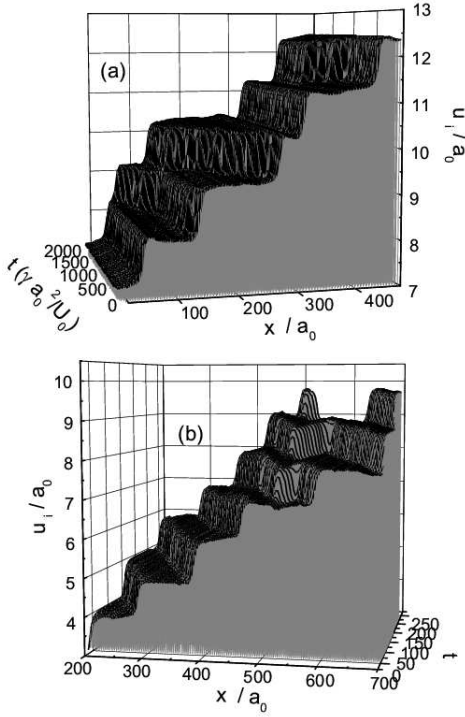
FIG. 14: (a) Evolution of displacements for $w/b_0 = 0.99$ and $f = 0.013 > f_s$ for $t > 0$. Defects at $x \approx 50a_0$, $x \approx 150a_0$ and $x \approx 325a_0$ are initially pinned while the others are mobile. A defect collision-release process occurs at $x \approx 150a_0$ and $t \approx 1500$. (b)Evolution of displacements when f is suddenly increased to $f = 0.048$. Nucleation is observed for $x \approx 500a_0$.

pinning starts with the defect at $x \simeq 270a_0$ and proceeds via a 'collision-release' process between the moving defect and its pinned neighbor. Thus, for $f \gtrsim f_s$ strong local variations in the defect mobility exist and the overall chain velocity depends strongly on the distribution $\{f_d\}$ (of which we show an example below). However, as seen in the v-f curves in Fig. 12, for $f \gtrsim 2f_d^{max}$ these effects vanish and the mobility approaches $dv/df \simeq c_d a_0 M_d$ with M_d the defect mobility without disorder. Another feature in the v-f curves for small defect densities is the velocity upturn at a force $f \simeq f_n^{min} < \mu$. It is caused by nucleation of *new defect pairs* in the incommensurate chain. The start of such a process is illustrated in Fig. 14(b): at $x \simeq 500a_0$ the chain is unstable against pair nucleation and the nucleated interstitials/vacancies are formed 'on top of' the moving incommensurate structure. This process only occurs at small defect densities when the time between passage of *existing* defects $\simeq 1/(v_d c_d)$ exceeds the nucleation time R_n^{-1}. For $f \gtrsim \mu$, the structure of both defects disappears again. The resulting dynamic state resembles that of the large velocity profile shown in Fig. 6, but with additional 'roughness' due to the weak CE disorder.

The v-f curves in Fig. 12 at $w/b_0 = 0.93$ and $w/b_0 = 1.1$, for which the defect density in the chain is larger, exhibit a smaller threshold force. In this regime the in-
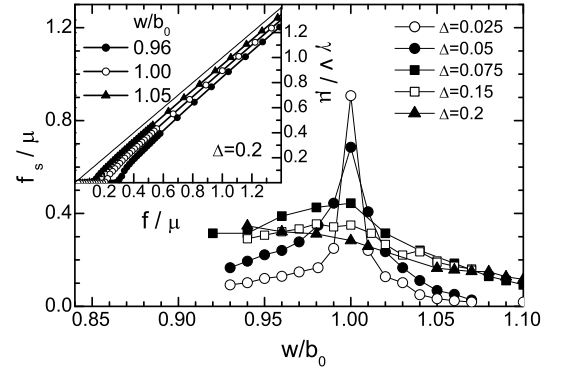
teraction between defects starts to become important and f_s is determined by *collective* pinning of the defects. This situation was studied analytically for the case of Josephson vortices in a disordered LJJ in [49]. We will not consider this situation explicitly but we note here that, as the disorder and the typical pinning force on the defects increases, the onset of the collective pinning regime shifts to larger defect density, where defect interactions are stronger [49].

In Fig. 15 we show the dependence of f_s on channel width, both for the weak disorder regime treated above and for larger disorder. The data at $\Delta = 0.025$ exhibit a sharp peak at $w = b_0$, reflecting the gap between minimum nucleation threshold and maximum defect pinning force. Larger disorder however rapidly smears the peak, being eventually completely suppressed for $\Delta \gtrsim 0.15$. The origin of this behavior is a spontaneous nucleation of defects in the static chain at larger disorder. This is conveniently illustrated via the changes in the distribution of the individual defect pinning force $\{f_d\}$ and that of the nucleation threshold $\{f_n\}$ for increasing disorder strength, shown in Fig. 16. The data were obtained by simulating hundreds of short channels ($L = 100a_0$) both with one vacancy, yielding $\{f_d\}$, and without 'geometric' defects, yielding $\{f_n\}$. While for $\Delta = 0.025$ the distributions are separated (formally, in infinite systems, such separation only exist for bounded disorder, see the next section), for larger disorder they start to overlap and they become nearly identical for $\Delta = 0.075$. This implies that nucleated defect pairs at $w = b_0$ can remain pinned, while at incommensurability defects may be nucleated before the 'geometrical' defects are released. In other words, regardless of the matching condition the *static* configuration contains both kinks and antikinks.

While for bounded disorder static defects first appear at a disorder strength defined as Δ_c, the complete collapse of the peak in f_s is associated with the presence of a *finite* density of disorder induced defects, of the order of the inverse kinkwidth $\sim l_d^{-1}$. We define the disorder
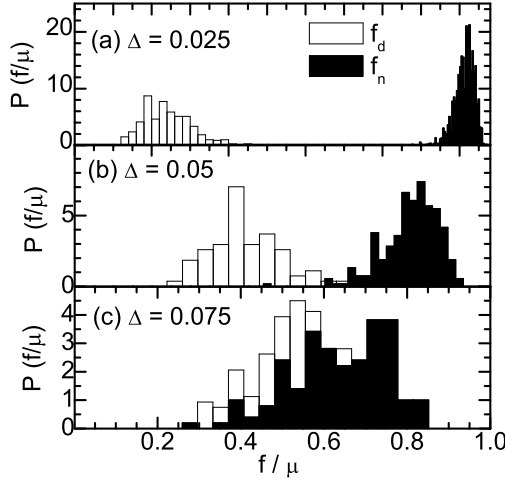
FIG. 16: Probability density of critical forces in channels of length $L = 100a_0 \approx 5l_d$ and $w = b_0$ for a commensurate chain (•) and for a chain with one vacancy (○) for $\Delta = 0.025$ (a), $\Delta = 0.05$ (b) and $\Delta = 0.075$ (c).
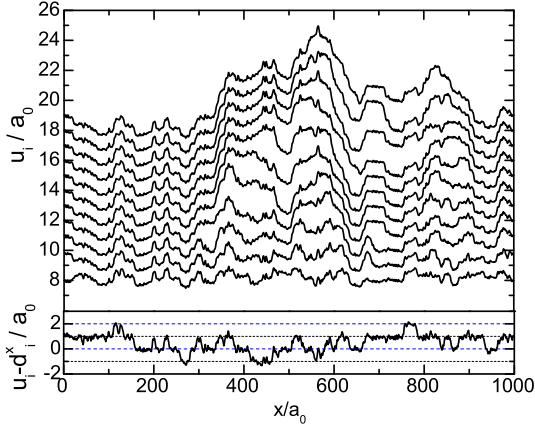

FIG. 17: Lower panel: relative displacements $u_i - d_i^x$ for $\Delta = 0.15$ and $f < f_s \simeq 0.0165$ at commensurability $w = b_0$. Upper panel: evolution of displacements at depinning, $f = 0.017$. The time increment between consecutive snapshots is $\Delta t = 10$ and for clarity each snapshot has been shifted up by a_0.

strength at which this occurs as Δ_*, here $\Delta_* \simeq 0.15$. An example of the displacement fields for this disorder strength is shown in Fig. 17 for $w = b_0$. The lower panel shows the displacements for $f \lesssim f_s$, relative to the displacements in the CE. Clearly, the static configuration has numerous defects. In general, the approach to the critical pinned state occurs by avalanches in which local nucleation and repinning, i.e. nonpersisting nucleation events, drive the rearrangements. The upper panel displays the evolution of displacements above threshold, revealing a growth of 'mountains' due to persistent nucleation, superimposed on a disordered background.

The effect of large disorder on the shape of the v-f curves is shown in the inset to Fig. 15. All curves now exhibit essentially linear behavior [57], except in a small

regime just above f_s. We note that also in this disordered regime a gradual transition to a smoother displacement field occurs at larger forces, similar to the dynamic transition found for CDW's. Going back to Fig. 15 we should also mention the overall asymmetry of f_s with respect to $w/b_0 = 1$ and the slight decrease of f_s on increasing w/b_0 at large disorder. These effects are unrelated to the competition between commensurability pinning and disorder discussed so far, but simply reflect the overal decrease of the edge potential for larger width.

C. Analysis of pinning forces and crossover to strong disorder

Using the results of Sec. V A, we now analyze in more detail the dependence of the pinning force on disorder and the vortex interaction range. We focus on the *average* pinning strength of isolated defects, which we derive here in a semi-quantitative fashion (the formal calculation is deferred to App. D). Our analysis applies to the case of weak disorder, i.e. we assume that the defect shape is unaffected by disorder [49]). Extrapolation to larger disorder provides a useful estimate for the crossover value Δ_* at which the commensurability peak vanishes. We conclude the section with a summary of previous results [33] for the threshold forces f_n^{min} and f_d^{max} in the special case of bounded disorder.

The disorder correction Eq.(34) to the energy of the vortex chain consists of a term H_a, due to amplitude fluctuations in the periodic potential, and a term H_s, due to random coupling to the strain. We first evaluate the typical pinning energy of a defect $\sqrt{\langle E_a^2 \rangle}$ due to the amplitude fluctuations. The local fluctuations are assumed to be uncorrelated on a length scale a_0, and have a variance $\langle (\delta\mu/k_0)^2 \rangle$. Hence, for a defect in the chain, which extends over a range l_d, the resulting random potential has a variance $\langle E_a^2 \rangle \simeq \langle (\delta\mu/k_0)^2 \rangle (l_d/a_0) \simeq \mu^2\Delta^2 l_d a_0/4$. The typical pinning force on a defect is then given by $\sqrt{\langle E_a^2 \rangle}/l_d$ which reduces to:

$$\sqrt{\langle f_a^2 \rangle} \simeq 0.2\mu\Delta g^{-1/4} \qquad (36)$$

The typical pinning energy $\sqrt{\langle E_s^2 \rangle}$ of a defect due to the term H_s in Eq.(34) is estimated in a similar way. The mean square energy due to coupling of a single fluctuation in V_s to the strain of a defect is $\sim \Gamma_s(0)(r_d/a_0)^2(2a_0/l_d)^2$ where r_d is the range of Γ_s, given below Eq.(34), and a_0/l_d represents the strain. On the scale of a defect, there are l_d/r_d such fluctuations. Thus the associated random potential for a defect has a variance $\langle E_s^2 \rangle \sim \Gamma_s(0)(r_d/a_0)^2(a_0/l_d)^2(l_d/r_d)$. Taking $\Gamma_s(0) \simeq \Gamma_l(0)$ and using Eq.(32), in which case $r_d = \lambda$, yields $\langle E_s^2 \rangle \simeq 2C_\alpha(U_0\Delta\lambda)^2(\lambda/a_0)^\alpha/(l_d a_0)$ (the factor 2 comes from the refined calculation in App. D) The typical pinning force $\sqrt{\langle E_s^2 \rangle}/l_d$ due to random coupling to the strain is then given by:

$$\sqrt{\langle f_s^2 \rangle} \simeq \sqrt{3C_\alpha}\mu\Delta(g/3\pi)^{\frac{2+\alpha}{2}}g^{-3/4} \qquad (37)$$

The ratio between the two characteristic defect energies is $\sqrt{\langle E_s^2 \rangle}/\sqrt{\langle E_a^2 \rangle} \simeq 8\sqrt{C_\alpha}(\lambda/a_0)^{\frac{\alpha+1}{2}}$, which shows that, particularly for increasing λ/a_0, the dominant pinning is due to random coupling to the strain. Henceforth we use only this contribution. We next estimate the disorder strength where the commensurability peak vanishes. As mentioned before, this collapse occurs when the density of disorder induced defects becomes $\sim l_d^{-1}$, in other words, when the typical energy gain of a defect due to disorder becomes of the same magnitude as its bare elastic energy $\int (dx/a_0)(\kappa_0/2)(\partial_x u)^2 \simeq \mu a_0 \sqrt{g}$. This leads to $\Delta_* \propto C_\alpha^{-1/2} g^{-(2\alpha+1)/4}$. For the particular case of random strains that are identical for all rows ($\alpha = 2$), Δ_* is given by:

$$\Delta_* \simeq 3g^{-5/4} \qquad (38)$$

This can be compared to the numerical data in Fig. 15. Even though those results were obtained for $\lambda/a_0 = 1$ ($g = 3\pi$), formally outside the regime of validity of our analysis, the predicted value $\Delta_* \simeq 0.18$ is in reasonable agreement with the data.

In the particular case of *bounded* random strains in the CE's, the distribution of the nucleation force $\{f_n\}$ at commensurability is bounded from below by f_n^{min} and that of the defect pinning force $\{f_d\}$ is bounded from above by f_d^{max} (at weak disorder). For completeness we give here the previously derived results [33] for these extremal values: both occur due to disorder fluctuations on the same length scale as that on which the displacement field $u(x)$ varies. For a defect this naturally corresponds to l_d. The associated maximum defect pinning force is $f_d^{max}/\mu \propto \Delta g^{3/2}$ (for uniform strains [33]). For nucleation, at $f \lesssim \mu$, the appropriate length scale is l_{san}, the extent of a so called small amplitude nucleus [39]. Due to the nonlinearity of the pinning force, l_{san} itself depends on the force, i.e. $l_{san}(f) > l_d$ and it diverges for $f \to \mu$. As shown in detail in [33], this leads to a minimum nucleation threshold given by $1 - (f_n^{min}/\mu) \propto [g^{3/2}\Delta]^{4/3}$. From the condition $f_d^{max} = f_n^{min}$ one then obtains the disorder strength Δ_c at which pinned defects can first appear spontaneously in the system: $\Delta_c \simeq g^{-3/2} < \Delta_*$.

VI. WIDE CHANNELS WITH WEAK DISORDER

We now consider how channels of larger width, in which vortices have the 2D degrees of freedom, behave in the presence of weak edge disorder. Close to commensurability, the effects we find are similar to that for a single chain. However, around 'half filling' the importance of the transverse degrees of freedom of the channel vortices become apparent.
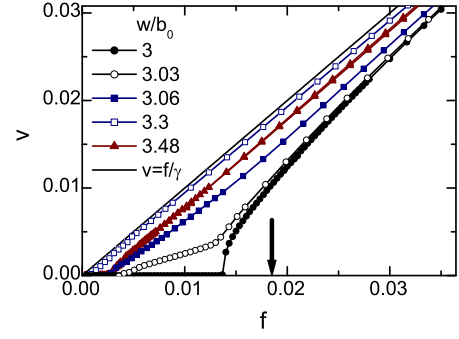

FIG. 18: v-f curves for weak disorder ($\Delta = 0.05$) and several channel widths. The arrow indicates the yield strength $f_s = \mu/3$ for $w/b_0 = 3$ and no disorder. All data are computed for channel lengths $L > 400a_0$.

A. Behavior near commensurability

For the commensurate case, $w/b_0 = n$, weak CE disorder causes a reduction of the threshold with respect to the ideal value $f_s^0 = \mu/n$, see the data in Fig. 18. The reduction originates from defect formation at threshold, as illustrated for $w = 3b_0$ in Fig. 19. In (a), three snapshots of the displacements of individual rows inside the channel are displayed. The first snapshot is for $f < f_s \simeq 0.7f_s^0$ and yields the 'flat' profile. The subsequent snapshots for $f > f_s$ reveal simultaneous nucleation and motion of a pair of 'oppositely charged' TSF's, each terminated at the CE's by a pair of edge dislocations (see Fig. 19(b)). The macroscopic, stationary motion of the array is governed by periodic repetition of this process at the least stable nucleation site. In (c) we show the vortex trajectories during nucleation of the TSF at the left in Figs. 19(a),(b). Very similar images were obtained in decoration experiments at the initial stage of VL depinning in NbSe$_2$ [11], implying that even for weakly disordered VL's, defects may nucleate at depinning (see also [12]). We also note that in simulations of a rapidly moving 2D vortex lattice [58] the same nucleation mechanism as in Fig. 19, but relative to the comoving frame, was identified as source of velocity differences between chains.

For incommensurate channels close to commensurability, the TSF's which are caused by the mismatch are pinned by the disorder. For the weak disorder strengths considered here the random stress from the CE's is not sufficient to break up the TSF's. Consequently, at zero drive the array in the channel consists of a weakly disordered superlattice of TSF's. The behavior of the transport curves is shown in Fig. 18 for $w/b_0 = 3.03$ and 3.06. It reveals features very similar to the curves of a single chain (Fig. 12). For $f_s \lesssim f \lesssim \mu/n$, a low mobility regime in the v-f curves develops due to the motion of the TSF's. Here f_s corresponds either to the rms pinning force of individual TSF's or to the collective pinning force for larger stack density. For forces $f > \mu/n$ the curves approach linear flow behavior again.
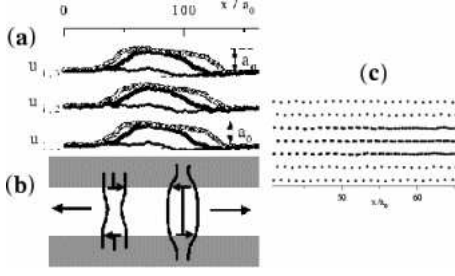
FIG. 19: (a): Time evolution of longitudinal displacements $u_{i,j}$ of individual rows $j = 1, 2, 3$ at depinning for $w/b_0 = 3$ and $\Delta = 0.05$. (b) Square lattice representation of the nucleated stacks of discommensurations. Small arrows indicate the Burgers vector of the dislocations terminating each stack. The large arrows indicate their propagation direction. (c) vortex trajectories during nucleation of the vacancy stack between $x = 40a_0$ and $x = 65a_0$ (up to the time corresponding to the filled symbols in (a)).
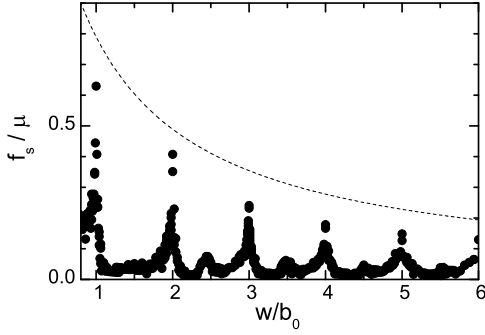

FIG. 20: Critical force versus channel width for a disorder strength $\Delta = 0.05$ using a velocity criterion $v \approx 0.01\mu/\gamma$. The dashed line represents the continuum result $f_s = \mu b_0/w$.

B. Behavior around 'half filling'

The dependence of f_s on the channel width for $\Delta = 0.05$ is shown in Fig. 20 for two disorder realizations. For larger channel widths, smaller channel lengths were used with $L \gtrsim 1000/(w/b_0)$. The data around matching ($w/b_0 \simeq n$) reflect the nucleation and pinning of TSF's as discussed above: f_s *at* commensurability is reduced compared to the pure value μ/n and the commensurability peak is considerably broadened, particularly for larger n, due to the pinning of TSF's. The apparent discontinuity in the peak may be an artifact of the finite channel length (see the discussion in Sec. V B on the distribution of nucleation sites). A new, and robust feature, however, is that around 'half filling' distinct maxima in f_s appear. The origin of these maxima is illustrated by the static structure near half filling. An example is given for $w/b_0 = 3.48$ in for Fig. 21. The triangulation shows that, in addition to aligned dislocations with $\vec{b} \parallel \vec{x}$, also misaligned dislocations appear with Burgers vector at an angle of about $\pm 60°$ with the CE's. These misaligned defects are locally stabilized by the disorder in the CE's and thus also

pinned by the disorder which leads to the increase in the threshold force. In addition, the projection of the driving force along the glide direction is always smaller for misaligned dislocations than for aligned dislocations. It is seen that the misaligned dislocations separate regions with n rows from regions with $n \pm 1$ rows. Either of these regions may thus be considered as a longitudinal stacking fault (LSF). In Sec. IV we mentioned that in absence of disorder LSF's are metastable, the structure with a single integer number of rows and a regular distribution of TSF's is energetically somewhat more favorable. In presence of weak disorder, however, the LSF are stable and have the lowest energy.

As for the dynamics at $f > f_s$, the dislocation structure and flow pattern are generally different from the static pattern of LSF's. We illustrate this in Fig. 22 where the vortex trajectories at various (increasing) driving forces are shown. For small drive (Fig. 22(a), $f \simeq 0.25\mu/(w/b_0)$), a region of plastic motion *within* the channel is seen at about the location where the static pattern shows a 4 row structure. Vortex transport through these fault zones occurs by repeated nucleation and annihilation of misaligned defects. At a fixed driving force an LSF remains at the same position, although its boundaries fluctuate over a distance of at most $2 - 3a_0$. This contrasts the situation in absence of disorder where LSF's can move along the channel via a 'climb' like process (see [35]).
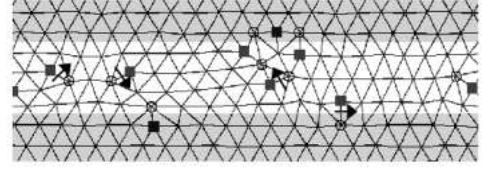
For different driving forces, the location and amount

FIG. 21: Triangulation of the static ground state structure for $w/b_0 = 3.48$ and $\Delta = 0.05$. The arrows indicate the Burgers vectors of the dislocations. Shown is a characteristic segment of the total channel length $L = 500a_0$.
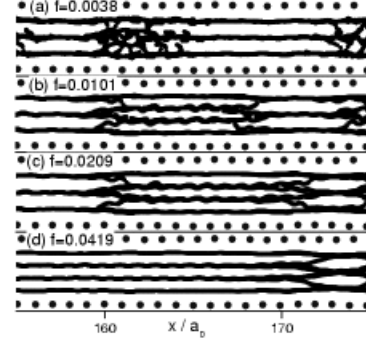

FIG. 22: Vortex trajectories for the channel segment shown in Fig. 21 ($w/b_0 = 3.48$, $\Delta = 0.05$) during motion over $\sim 4a_0$ at (a) $f = 0.0038$, (b) $f = 0.0101$, (c) $f = 0.0209$ and (d) $f = 0.0419$.

of either n or $n \pm 1$-row regions or fault zones is different, as shown in Figs. (b),(c) and (d). In this particular segment the $n = 4$ region expands on increasing drive but at other locations the reverse can occur. Moreover, after cycling the force, a different structure can occur at the same drive, i.e. no unique structure exists at a given force. This may also lead to small hysteresis in the *v-f curves*. Overall, we see that the transverse degrees of freedom in the channel, in combination with disorder, give rise to an important new mechanism of yield strength enhancement. In the following section we analyze these structures in more detail in the context of strong disorder.

VII. WIDE CHANNELS WITH STRONG DISORDER

The behavior of f_s versus w/b_0 in Fig. 20 still exhibits considerable discrepancies with the experimental data in Fig. 2. Clearly, the CE disorder underlying these experimental data (see [59]) differs from the type of weak CE disorder considered so far. Motivated by recent imaging experiments [34], which showed glassy vortex configurations in the NbN edge material, we now consider the case of strong CE disorder. As will be shown, in this regime the effect of transverse degrees of freedom and the presence of misaligned defects provide the main mechanism for the critical current oscillations.

The simulations we discuss here in detail were performed at a large disorder strength $\Delta = 0.2$. The only remaining order in the CE arrays is their preferred orientation with the principle lattice vector along the CE's. The system sizes were typically such that $wL \gtrsim 1500a_0b_0$. We also allowed for quenched defects between the two CE's (uncorrelated longitudinal strains in the upper and lower CE arrays), but at these large disorder strengths this is not essential.

A. Static structures, yield strength and depinning

In Fig. 23 we show triangulations of the static vortex configuration for channels of width $w/b_0 = 3$, $w/b_0 = 3.5$ and $w/b_0 = 4$. As seen in Figs.(a) and (c), even in the matching case dislocations are present due to the large random stresses from the CE. While some of these may originate from quenched 'phase slips' between upper and lower CE's, we checked that, also without these 'phase slips', the matching structure at this disorder strength always exhibits twisted bonds (defined by two adjacent dislocations of opposite charge) at the CE's as well as oppositely 'charged' TSF's terminated by defect pairs at the CE. While most defects are thus situated along the CE with $\vec{b} \parallel \vec{x}$, occasionally they can be located inside the channel and have misoriented Burgers vector. Turning to the mismatch case in (b), it is seen that a region of 4 rows (left) coexists with a 3 row region (right). In
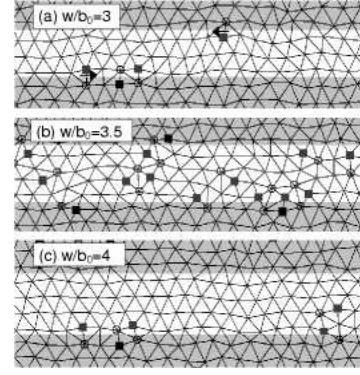

FIG. 23: Delauney triangulation of the ground state structure at $\Delta = 0.2$ for (a) $w/b_0 = 3$, (b) $w/b_0 = 3.5$ and (c) $w/b_0 = 4$. The arrows in (a) indicate the Burgers vectors of the dislocations. The aligned dislocations in (a) and (c) include a disorder induced static dislocation pair (twisted bond) at the lower CE, in (b) numerous misaligned dislocations are present.
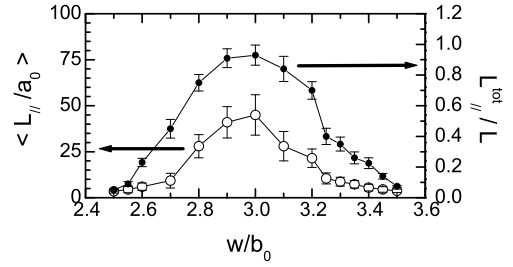

FIG. 24: The 'correlation' length $\langle L_{//} \rangle$ (○) and the fraction $L_{//}^{tot}/L$ (●) of regions with $n = 3$ rows versus w/b_0.

between these regions, there must be dislocations with misaligned Burgers vectors. In addition, numerous other misaligned defects are visible, rendering local destruction of the chain alignment with the CE's (although less frequent, the latter can also occur in the matching state, see Fig. (c)).

To further characterize the disorder in the $f = 0$ structures, we analyzed, for the regime $2.5 < w/b_0 < 3.5$, the average length of domains without misaligned dislocations, $\langle L_{//} \rangle$, as well as the total fraction, $L_{//}^{tot}/L$, of regions with $n = 3$ rows. The results are shown in Fig. 24. As observed, both quantities are maximum at $w/b_0 = 3$ and decay considerably away from matching: for $|w/b_0 - 3| > 0.3$ the average length of 'correlated' $n = 3$ regions in the static structure is no more than $10a_0$ and they make up less than $\sim 50\%$ of the channel. The remaining fraction $1 - (L_{//}^{tot}/L)$ contains misaligned dislocations and small regions with 2 ($w/b_0 \simeq 2.5$) or 4 (for $w/b_0 \simeq 3.5$) aligned chains.

In Fig. 25 we show the behavior of the threshold force for $\Delta = 0.2$. The modulation of f_s with channel width is still present but it has changed considerably compared to the weak disorder case. The sharp maxima at integer w/b_0 have vanished, very similar to
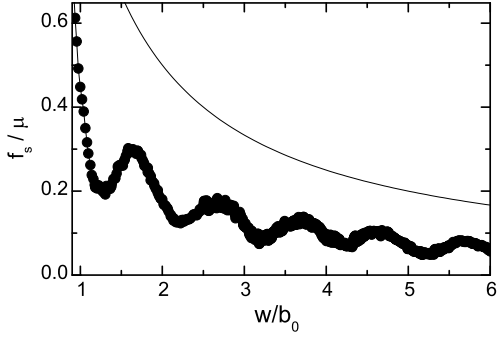
FIG. 25: Computed threshold force versus channel width for strong disorder, $\Delta = 0.2$. The data were obtained by taking the friction force $f - \gamma v$ at a velocity criterion $v \simeq 0.025(\mu/\gamma)$ and subsequent averaging and smoothing over 5 disorder realizations. Drawn line: continuum result, $f_s = \mu/(w/b_0)$.
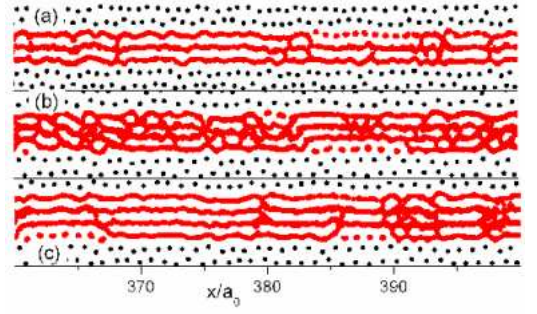

FIG. 26: Vortex trajectories at small velocity $v \simeq 0.001$ for: (a) $w/b_0 = 3.1$ ($f = 0.0053 \simeq 0.1\mu$), (b) $w/b_0 = 3.6$ ($f = 0.0074 \simeq 0.14\mu$) and (c) $w/b_0 = 4.1$ ($f = 0.0044 \simeq 0.08\mu$), all during motion over $\sim 3a_0$.

the case of the 1D chain at strong disorder, see Fig. 15. Instead, we now observe smooth oscillations, with maxima in f_s for $w/b_0 \simeq n + 0.65$ and minima for $w/b_0 \simeq n + 0.15$. The maxima, although occurring slightly above 'half filling', are of similar nature as the local maxima at $w/b_0 \simeq n \pm 1/2$ for weak disorder: they are related to numerous misaligned defects present in the structure around mismatch. They enhance the flow stress compared to that of the structures around matching with predominantly aligned defects.

The differences in threshold force are also reflected by the vortex trajectories at small velocity. In Fig. 26 we show these trajectories for channel widths $w/b_0 = 3.1$, 3.6 and 4.1, close to the extrema in f_s. The first thing to notice is that the trajectories at mismatch (Fig.26(b), $w/b_0 = 3.6$) are densely interconnecting, on a scale $\sim a_0$, i.e. the motion is fully plastic and creation and annihilation of misaligned defects occurs over nearly the full channel length. For the 'near matching' cases in (a) and (c), the motion occurs mainly in the form of integer chains. However, for the small velocity considered here, the dynamics still exhibits a considerable amount of plastic motion. This partly occurs due to vortices which remain stuck at the CE's (also visible in (b)) and partly due to narrow interconnecting regions. In fact, comparing the average length of the regions without inter row switching in (a) with the data for the static structure in Fig. 24, it is seen that near matching the structure at small v is more disordered than the corresponding static structure, reflecting nucleation of misaligned defects in regions which were free of such defects at $f = 0$.

B. Analysis of dynamic properties

We now consider in more detail the properties of the moving structures at $f > f_s$. We first show in Fig. 27(a) two characteristic v-f curves associated with a minimum ($w/b_0 = 3.1$) and a maximum ($w/b_0 = 3.6$) in flow stress.
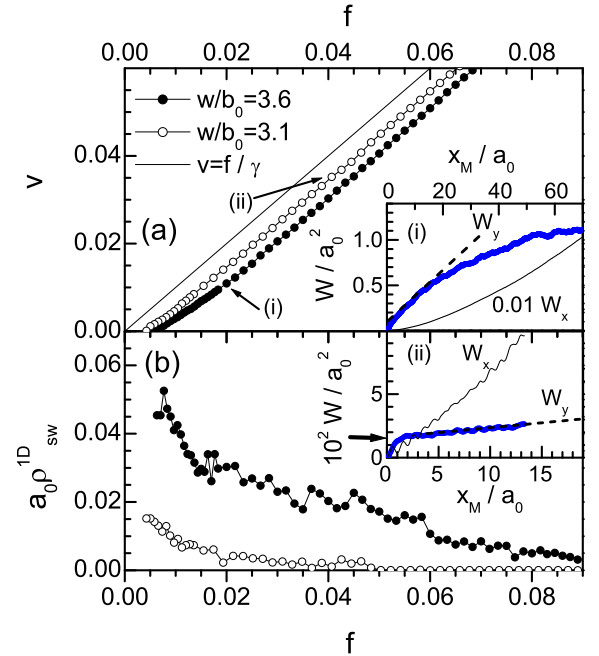
FIG. 27: (a) v-f curves around a minimum in flow stress $w/b_0 = 3.1$ (○), and around a maximum $w/b_0 = 3.6$ (●). Inset: $W_x(x_M)$ and $W_y(x_M)$ for $w/b_0 = 3.6$ and $f = 0.021$. The dashed line emphasizes the linear behavior of W_y in the regime $3a_0 < x_M < 10a_0$. (b) The density of switching points $\rho_{sw}^{1D} \equiv \Delta W_y/(\Delta x_M a_0^2)$ versus force for $w/b_0 = 3.1$ (○) and $w/b_0 = 3.6$ (●). Inset: $W_x(x_M)$ and $W_y(x_M)$ for $w/b_0 = 3.1$ and $f = 0.041$. The arrow indicates the value $W_{y,c}$ referred to in the text.

It is observed that the enhanced threshold in the latter case also translates in a larger dynamic friction, $f - \gamma v$, of the driven structure. In addition, the latter curve exhibits a small positive curvature in the small velocity regime $v \lesssim 0.01$. This nonlinearity is related to the strong plastic nature of the motion in this regime.

A convenient way to characterize the amount of plasticity is to calculate the mean square displacement of

vortices form their center of mass (M) positions [60]:

$$W_\alpha(t) = \sum_i [\alpha_i(t + t_0) - \alpha_i(t_0)]^2 / N_{ch}, \qquad (39)$$

where $\alpha = x - x_M, y - y_M$ denotes longitudinal and transverse displacements, respectively. As shown by Kolton *et al* for a 'bulk' 2D vortex lattice [60], $W_\alpha(t)$ can be characterized by $W_\alpha = R_\alpha t^{\xi_\alpha}$. For example, when $\xi_y = 1$ we have normal transverse diffusion (caused by 'random' switching of vortices between chains) with $R_y = D_y$ the diffusion coefficient. However, in the channels W_y will become bounded at long times (large x_M) due to the finite channel width. In the inset (i) to Fig. 27(a) we have illustrated this behavior for $w/b_0 = 3.6$ and $f = 0.021$. For $x_M \lesssim 15a_0$ (the point $x_M = 0$ was chosen in the steady state after transients had disappeared), W_y increases linearly as in usual diffusion, but for larger displacements (times) W_y levels off and eventually saturates. In addition, even when all vortices remain in their chain (no transverse diffusion), W_y initially increases to a value $W_{y,c}$ due to finite chain 'roughness'. Such behavior is observed for $x_M \lesssim 2a_0$ in the inset (ii) to Fig. 27(b) where W_y is shown for a more coherent flow situation at $w/b_0 = 3.1$ and $f = 0.041$. In practice, we found that $W_{y,c}$ is always reached for $x_M < 3a_0$, while for the long time (large distance) behavior significant levelling of W_y occurs only when $x_M \gtrsim 10a_0$. The appropriate regime we use to characterize real diffusion is therefore given by $3a_0 < x_M < 10a_0$ (i.e. $\Delta x_M = 7a_0$). Further, D_y itself does not directly reflect the density of chain-switching points along the channel. Defining the '1D' density of such switching points as $\rho_{sw}^{1D} \simeq N_{sw}/L$, the *rate* of switching increases linearly both with ρ_{sw}^{1D} and with the average velocity: $t_{sw}^{-1} \simeq \rho_{sw}^{1D} v$. Hence, the diffusion constant is given by: $D_y \simeq a_0^2/t_{sw} = \rho_{sw}^{1D} v a_0^2$. Being interested in ρ_{sw}^{1D}, we therefore divide out the intrinsic velocity dependence of D_y and calculate $W_y(t)/(v t a_0^2) = \Delta W_y/(\Delta x_M a_0^2) \equiv \rho_{sw}^{1D}$.

The results of ρ_{sw}^{1D} versus f are shown in Fig. 27(b) for the two cases $w/b_0 = 3.1$ and $w/b_0 = 3.6$. Around the minimum in flow stress ($\circ$), the overall value of ρ_{sw}^{1D} is considerably smaller than around the maximum ($\bullet$), similar to what is seen in the trajectories in Fig. 26. For both cases, ρ_{sw}^{1D} is clearly reduced on increasing the force. This reflects both a decrease of the number of fault zones in the moving structure as well as a suppression of switch events (called 'transverse freezing' in [60]) within regions already organized in n moving rows. Around matching, ρ_{sw}^{1D} smoothly vanishes at $f \sim \mu \approx 0.05$, indicating complete dynamic ordering into an $n = 3$ row structure without transverse wandering. For $w/b_0 = 3.6$ an ordering transition is also observed but it occurs at much larger drive ($f \sim 3\mu$, not shown) and the array orders into an $n = 4$ row configuration, with a reduced spacing $b < b_0$ between the chains and average vortex spacing $a > a_0$ within the chains. At the end of this section we will show how in this large drive regime the number of rows changes with w/b_0.
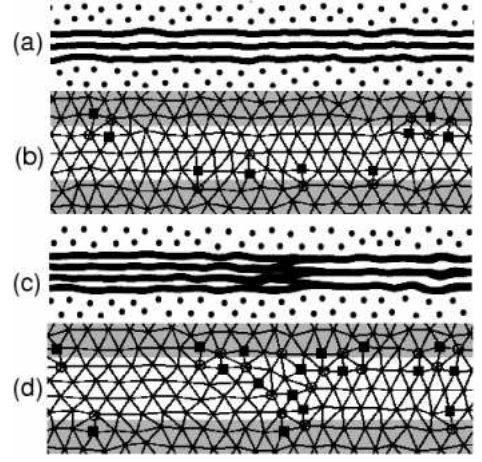

FIG. 28: (a) Flow trajectories at large drive (a) during motion over $\sim 3a_0$ for $w/b_0 = 3.1$ and $f \simeq 2\mu$. (b) Delauney triangulation of one snapshot of (a). (c) Trajectories for $w/b_0 = 3.55$ and $f \simeq 2\mu$. (d) Triangulation of a snapshot of (c).

The insets to Fig. 27 also show the longitudinal mean square displacements. For strongly plastic flow at mismatch (inset (i)), W_x is large and ξ_x is close to 2, as expected when some vortices remain stuck at the CE's. For the more coherent situation in (ii), where transverse switching has nearly ceased, W_x is smaller and $\xi_x \gtrsim 1$. We always find an exponent $1 < \xi_x < 2$, similar to the results for 2D VL's in [60]. Interestingly, even without transverse wandering ($\rho_{sw}^{1D} = 0$), W_x increases indefinitely (with $\xi \gtrsim 1$), indicating that the moving integer chain structure still exhibits slip events and (local) velocity differences between the chains.

We illustrate some more aspects of the structures at large drive in Fig. 28, where the vortex trajectories and triangulations of a single snapshot are displayed for $w/b_0 = 3.1$ and $w/b_0 = 3.55$, both at $f \simeq 2\mu$. For $w/b_0 = 3.1$, we do not see any transverse wandering in Fig. 28(a). Figure 28(b) shows that in this case the dynamic structure exhibits only dislocations with $\vec{b} \parallel \vec{x}$, mainly located at the CE but also occasionally between chains inside the channel. The latter dislocations are possibly dynamically nucleated. They are non-stationary in the comoving frame and lead to slip events and the growth of W_x as was discussed above. Turning to the mismatch case (Figs. 28(c) and (d)), it is seen that the dynamic structure consists of $n = 3$ and $n = 4$ row regions coexisting in the channel. At the driving force considered here, ρ_{sw}^{1D} has a finite but small value $a_0 \rho_{sw}^{1D} \simeq 0.007$, which is solely due to switching of vortices in the fault zones separating the 3 and 4-row regions. *Within* these regions transverse wandering is absent. At yet larger forces the minority 3-row regions vanish and complete ordering into 4 rows occurs, as for the case $w/b_0 = 3.6$. For a given driving force, the n-row regions again remain quasi-static during motion. The triangulation in (d) exhibits the expected misaligned dislocations at the fault

zone but in general also aligned dislocations are present between the chains within an n-row region (not shown in the figure).

It is also interesting to compare the velocities in the two coexisting regions with n and $n \pm 1$ rows. Denoting the vortex velocity in an n-row region by v_n and the longitudinal vortex spacing there by a_n, flux conservation implies that $n v_n / a_n = n' v_{n'} / a_{n'}$. We checked that, in both regions, the average flux density $1/(a_n b_n)$, with $b_n = w/n$ the row spacing, was equal to $1/(a_0 b_0)$ within $\sim 4\%$. Therefore $a_{n'} = (n'/n) a_n$, and consequently the average vortex velocities are equal, $v_n = v_{n'}$. However, the local *washboard frequency*, $\nu_n = v_n / a_n$, is different in both regions. Indeed, the spectrum of the velocity fluctuations in channels with dynamic coexistence of n and $n \pm 1$ rows showed two shallow fundamental peaks at frequencies $\nu_n / \nu_{n'} = n'/n$. We however note that, both around matching (where a single peak occurs at $\nu \sim v/a_0$) and around mismatch, the amplitude of the washboard peak(s) decays on increasing the channel length L. In addition, for large velocities the mixed $n/n \pm 1$ structures ultimately anneal into a single n or $n \pm 1$ domain, causing the collapse of one of the peaks.

The simulations also allow to explicitly show the influence of the transverse degrees of freedom on the modulations of the dynamic friction force (and, ultimately, the critical current). Generalizing the expression for the friction force Eq.(20) in Sec. III B including transverse fluctuations leads to:

$$
\begin{aligned}
f & = (\gamma/v)[\langle (\partial_t u_x)^2 \rangle_{i,t} + \langle (\partial_t u_y)^2 \rangle_{i,t}] \\
& = \gamma v + f_{fric}^x + f_{fric}^y \\
& \equiv \gamma v + f_{fric},
\end{aligned} \tag{40}
$$

where f_{fric}^x and f_{fric}^y denote the contribution to the total friction due to longitudinal and transverse fluctuations, respectively. Figure 29(a) displays the numerical results for these quantities, normalized by the total friction force $f - \gamma v$ as obtained from the $v - f$ curves. The sum of the two data is 1 as it should be, confirming the correct numerical evaluation of these quantities. The total friction is also shown for clarity (Fig.(b)) and is essentially the same as the data shown in Fig. 25. Clearly, the *relative* contribution of longitudinal fluctuations to f_{fric} *decreases* on approaching a mismatch situation, while f_{fric}^y / f_{fric} increases accordingly. These qualitative features remain present also at larger velocities, where permeation modes between chains are being suppressed.

Finally, we consider the continuous modulation of structural (dis)order in the moving arrays when varying the channel width. As was shown in Fig. 27(b), for a fixed velocity, the density of switching points ρ_{sw}^{1D} is maximum around mismatch while for fixed channel width it decreases with velocity. We can then define an ordering velocity v_c operationally as the point at which ρ_{sw}^{1D} is reduced below a certain threshold. In Fig. 29(c) the behavior of v_c for channel widths $w/b_0 > 2$ is shown for two criteria. The lower curve ($v_{c,1}$), with $a_0 \rho_{sw}^{1D} \approx 0.01$, corresponds to a situation with $\sim 70\%$ of the channel length
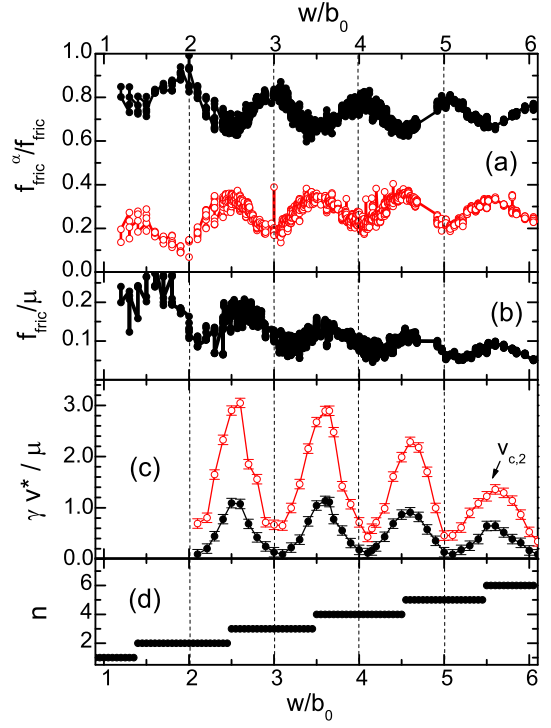

FIG. 29: (a) The contributions f_{fric}^x / f_{fric} ($\bullet$) and f_{fric}^y / f_{fric} ($\circ$) to the dynamic friction versus w/b_0 for a velocity $v = 0.1\mu/\gamma$. (b) Total friction $f - \gamma v$ at $v = 0.1\mu/\gamma$. (c) Ordering velocity $v_{c,1}$ ($\bullet$) determined from a criterion $a_0 \rho_{sw}^{1D} \simeq 0.01$, and $v_{c,2}$ ($\circ$) using a criterion $a_0 \rho_{sw}^{1D} \simeq 0.002$ (error bars were estimated from different disorder realizations). (d) Number of moving rows n at large drive ($v \gtrsim v_{c,2}$) versus w/b_0.

'transversely frozen' into integer chain regions of length $\gtrsim 10 a_0$. The upper curve ($v_{c,2}$), with $a_0 \rho_{sw}^{1D} \approx 0.002$, corresponds to nearly fully annealed arrays. As observed, $v_{c,1}$ increases smoothly by about an order of magnitude between a matching and mismatching situation, while $v_{c,2}$ increases by a factor $\gtrsim 5$ (except for $w/b_0 > 5$). Regardless of the criterion, the amplitude of the modulation of v_c is considerably larger than the amplitude of the f_s modulation, which we will further discuss shortly.

For $v \gtrsim v_{c,2}$ the arrays all completely anneal into a single n-row structure without permeation modes. Figure 29(d) displays the number of rows n of these structures versus w/b_0. The switching from n to $n + 1$ rows is seen to occur at half integer channel widths for $w/b_0 > 3$ but the transitions $1 \to 2$ and $2 \to 3$ take place below these points, at $w/b_0 \simeq 1.35$ and $w/b_0 \simeq 2.4$, respectively. Around the transition points, there are regions in which n and $n \pm 1$ rows coexist at smaller velocity $v \lesssim v_{c,2}$. The widths of these regions were found to be $\Delta w/b_0 = \pm 0.05$.

VIII. DISCUSSION

The results for f_s versus w/b_0 at strong disorder in the previous section show strong resemblance to the measure-
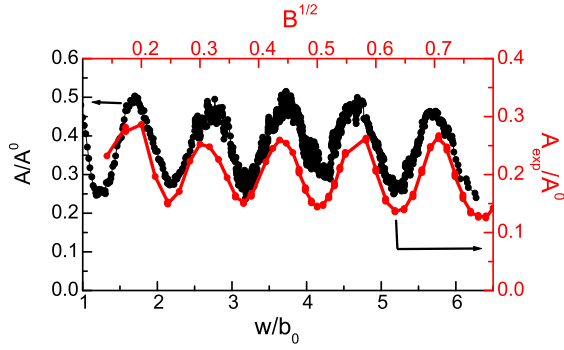
FIG. 30: Comparison between the experimentally measured yield strength of an artificial flow channel and the numerical results at strong disorder [61], represented through the parameter A (see the text) normalized by the value $A^0 = (\pi\sqrt{3})^{-1}$ for the ideal lattice.

ments of the critical current versus field B in the experimental channel system, see Fig. 2. For a more detailed comparison, we combine in Fig. 30 both data, represented in terms of the parameter A (see Sec.I): for the experiment, A_{exp} is determined from $A_{exp} = F_s w/(2c_{66})$ and is plotted versus $B^{1/2}$, for the simulations, $A = (f_s/\mu)(w/b_0)A^0$ ([61]). As observed, the shapes of the oscillations are in very reasonable agreement, although the overall value of A from the numerics is larger than the experimental value [62]. The important conclusion from the simulations here is thus that the maxima in the measured critical current do not correspond to traditional commensurability peaks, but are caused by enhanced plastic motion and transverse deviations in mismatching channels with strong edge disorder. Previously, we indeed obtained experimental evidence for this mechanism via mode-locking (ML) experiments [31] in which an rf-drive is superimposed on the dc-drive. Interference between the former and collective modes of deformation in the moving array leads to plateaus in the current-voltage curves. The plateau (ML) voltage then directly yields the number of moving rows n and transitions from $n \to n \pm 1$ rows were observed to coincide with maxima in critical current [63].

More detailed ML-experiments provided a wealth of additional information on the dynamics of the arrays [32]. In particular, a minimum velocity was required to observe the ML-phenomenon, which we identified as ordering velocity. This ordering velocity exhibited a strong upturn away from matching, similar to the behavior of v_c in the simulations. As proposed in [32], v_c can be estimated from a modified version of the dynamic ordering theory of Koshelev and Vinokur (KV) [37]. Firstly, instead of the 2D random potential in [37], for the channels v_c is related to the short range correlated random stress from the CE, with r.m.s. amplitude $\sim \varepsilon_{ce}c_{66}$ and ε_{ce} the random strain. Secondly, when thermal fluctuations can be ignored compared to typical defect energies (see below), v_c is inversely proportional to

the energy $k_B T_p$ for creation of small defect pairs (see also [64]): $v_c/a \simeq \sqrt{3/32\pi}(a_0/a)^2(\varepsilon_{ce}c_{66})^2 a_0 b_0/(\gamma k_B \bar{T}_p)$, with $k_B \bar{T}_p \simeq A_p c_{66} a_0^2/2\pi$ (per unit vortex length). The typical pairs referred to are those with misaligned Burgers vector, which are responsible for breakup of the chain structure. Hence, the increase of v_c away from matching implies a decrease in the pair formation energy, which is accounted for by including the parameter $A_p \lesssim 1$ in $k_B \bar{T}_p$, while setting $A_p \equiv 1$ at matching. Experimentally, A_p decreased to ~ 0.1 at mismatch. The behavior of v_c and A_p in the simulations is analyzed using the dimensionless form of the above formula for v_c:

$$(\gamma v_c/\mu) \simeq 2.5\varepsilon_{ce}^2(a_0/a)/A_p \qquad (41)$$

The data for $v_{c,1}$ around matching (where $A_p = 1$) yield as measure for the random strain $\varepsilon_{ce} \simeq 0.19$ and, near mismatch, a reduction of the defect pair creation energy by a factor $A_p \simeq 0.1$. The latter is in very reasonable agreement with the experiments, and the reduction of $k_B T_p$ near mismatch also qualitatively agrees with the large number of disorder induced fault zones observed in the static structures near mismatch (Fig.23). However, the result for ε_{ce} is considerably larger than the value $\varepsilon_{ce} = 0.025$ found experimentally. This is also manifest in the fact that in the experiments the pinning frequency, defined as $f_s/(\gamma a)$, always exceeds the ordering frequency v_c/a, while in the simulations $f_s \lesssim \gamma v_c$.

Within the modified KV theory, the pinning frequency and the ordering frequency are directly related via [32]: $v_c/a = \tau(f_s/\gamma a)^2$ with $\tau = (\varepsilon_{ce}^2/2A^2)(wB)^2/(A_p c_{66}\rho_f)$. Experimentally, τ was found to be independent of the matching condition. The decrease in the defect pair creation energy ($\propto A_p$) then relates to the increase in the pinning frequency (yield strength) away from matching ($\propto A$) as $A_p \propto 1/A^2$. The numerical results for A_p versus A behave similarly and can be fitted by $A_p \propto 1/A^\varsigma$ with $\varsigma \sim 2 - 3$, but data collected over the full range of w/b_0 show to much scatter to make a more detailed comparison. Nevertheless, the KV model qualitatively accounts for the enhanced amplitude of the v_c modulation compared to that of the yield strength.

As for the discrepancy between the experimental and numerical values for ε_{ce} or v_c, one should keep in mind that experimentally the ordering velocity is determined from the onset of an n-row ML plateau, i.e. it corresponds to the velocity at which coherent n-row regions first appear, while incoherent regions may still exist in other parts of the channel. In the simulations this may thus correspond to v_c determined using a larger criterion for the density of switching points ρ_{sw}^{1D}. In addition, the superimposed rf-drive in the experiments may assist re-ordering of the structure, also leading to smaller values of v_c. For future studies it is interesting to directly compare numerical simulations of channels with mixed rf-dc drive with the experiments and test which criterion best represents the reordering phenomenon.

Additionally, the experimental results indicated that in the large drive regime (where the ML amplitude satu-

rates at a constant value), the coherently moving fraction of vortices does not exceed $\sim 40\%$ (at matching), while it was reduced on approaching mismatch. This feature appears at odds with the simulations where eventually the arrays all order into a completely transversely frozen n-row domain at large drive, regardless of the matching condition. At present we do not have a good explanation for this discrepancy.

Finally we comment on the $T = 0$ approximation made throughout this study. When thermal fluctuations are important, not only does one expect the dynamic ordering behavior to be changed (see [37, 65]), also the sharp threshold behavior in the v-f curves will be smeared and activated flow may occur. The relevant energy scale for both phenomena is again the energy for formation of small defect pairs $k_B T_p$. In the low magnetic field experiments in [32] this energy was ~ 2 orders of magnitude larger than $k_B T$ and for comparison with these results the $T = 0$ approximation is justified. To compare with the experiments near the melting field in [65], it would be required to include thermal fluctuations in the simulations.

IX. SUMMARY

We have presented a detailed study of the properties of vortices confined to narrow flow channels with pinned vortices in the channel edges. In the experimental system which motivated this work [29, 31, 32], the threshold force (yield strength) shows pronounced commensurability oscillations when the natural vortex row spacing is varied through integer fractions of the channel width. The analysis and simulations presented in this paper show that in a mesoscopic channel system the dependence of threshold on commensurability as well as the dynamics of vortices in the channels drastically vary with the amount of disorder in the confining arrays. At zero or weak disorder the system behaves similar to 1D LJJ-systems and defects at the CE's reduce the yield strength. At large disorder the behavior involves transitions from quasi-1D to 2D structures, where an increase in the amount of plastic deformations enhances the yield strength similar to the situation in the classical peak effect in superconductors.

We first presented a generalized sine-Gordon description for a 1D vortex chain in an ideally ordered channel. In this case (or for channels with multiple chains near commensurability) the threshold force has sharp peaks at commensurate widths, whereas it is essentially vanishing at incommensurability due to easy glide of 'aligned' defects, i.e. defects with Burgers vector along the CE. The model was then extended to study the effects of weak disorder in the confining arrays. Simulations and analytical results showed that this disorder causes the sharp maxima in the threshold force at matching to be lowered and broadened due to nucleation (at matching) and pinning(at mismatch) of edge defects. Apart from these de-

fects, the arrays respond elastically in this regime, both near threshold and at large drive. We studied numerically the relevant edge defect dynamics and, using the sine-Gordon model, we analyzed the crossover to strong defect pinning on increasing the disorder strength.

For large disorder in the CE's, matching between the longitudinal vortex spacings in and outside the channel becomes irrelevant and the peaks in threshold force around matching completely vanish with a 'saturated' value for f_s of about 30% of the ideal lattice strength. Around mismatch however, the arrays become susceptible to formation of defects with Burgers vector misoriented with the channel direction. Such defects either locally break up the integer chain structure or exist at the boundaries of n and $n \pm 1$-row regions coexisting in the channel. At large disorder, they are strongly pinned and cause the threshold force to exceed that around matching. Approaching a matching condition, the density of misaligned defects is reduced and a smooth modulation of f_s results, with minima near matching. The depinning transition always involves plastic deformations *inside* the channel, but the amount of plasticity drastically increases away from matching. Using the density of transverse switching points (obtained from the transverse diffusion in the moving structures) as dynamic 'order parameter', we study the evolution of the moving structures on changing the channel width and the drive. The arrays reorder (partially) into transversely frozen n-row regions at a velocity v_c which shows a similar modulation with commensurability as the threshold force. Finally, we compared the modulations of f_s and v_c at strong disorder with the available experimental results and with the dynamic ordering theory in [37] and find good qualitative agreement.

APPENDIX A: ORDERED CHANNEL FOR ARBITRARY FIELD

In this appendix we calculate the edge potential and sine-Gordon parameters in a symmetric, ordered channel with $w \simeq b_0$ for arbitrary field. The interaction between a vortex at $\mathbf{r} = (x, y)$ in the channel and the pinned vortices in the CE's at $\mathbf{R}_{n,m}$ is given by:

$$V_{ce}(\mathbf{r}) = (2\pi)^{-2} \int d\mathbf{k} \sum_{n,m} V(\mathbf{k}) e^{i\mathbf{k}\cdot(\mathbf{r}-\mathbf{R}_{n,m})}, \quad (A1)$$

where $V(\mathbf{k})$ is the Fourier transform of the vortex-vortex interaction. To obtain an expression valid over larger range of fields than the (low field) London-regime, we use

a generalization of the London potential Eq.(6) as proposed by Brandt [30]. This generalization accounts for the reduction of superfluid density with field and an additional attractive interaction due to overlapping vortex cores. The Fourier transform of this interaction reads:

$$V(\mathbf{k}) = 2\pi U_0 (1-b) \left[\frac{1}{|\mathbf{k}|^2 + \lambda'^{-2}} - \frac{1}{|\mathbf{k}|^2 + \xi'^{-2}} \right], \text{(A2)}$$

where $b = B/B_{c2}$, $\lambda' = \lambda/(1-b)^{1/2}$ and $\xi' = \xi\frac{C}{(2-2b)^{1/2}}$ the effective coherence length with $C \sim 1$. It is convenient to split Eq.(A1) for the total potential in terms of the contribution V_m of row m (see Fig. 3). Integrating over k_y and using Poisson summation yields

$$V_m(\mathbf{r}) = \sum_l |V_m^l(y)| \cos l k_0 (x - m a_0/2) \qquad \text{(A3)}$$

where $k_0 = 2\pi/a_0$ and the prefactors are:

$$|V_m^l(y)| = k_0 U_0 (1-b) \left[\frac{e^{-\overline{lk_{0,\lambda'}}|y_m'|}}{\overline{lk_{0,\lambda'}}} - \frac{e^{-\overline{lk_{0,\xi'}}|y_m'|}}{\overline{lk_{0,\xi'}}} \right] \text{(A4)}$$

with $\overline{lk_{0,\lambda'}} = \sqrt{(lk_0)^2 + (\lambda')^{-2}}$, $\overline{lk_{0,\xi'}} = \sqrt{(lk_0)^2 + (\xi')^{-2}}$ and $y_m' = -y + m[b_0 + ((w-b_0)/2|m|)]$. First of all, we neglect in Eq.(A3) the $l = 0$ terms which represent uniform (x-independent) interaction. Secondly, when $\lambda \gtrsim a_0$, as practically encountered in films, $\overline{k_{0,\lambda'}} \approx k_0$. Then the $|l| > 1$ terms can be neglected, resulting in a sinusoidal potential $|l| = 1$. Further, in the summation over m only the contributions from the $m = \pm 1$ terms are significant. Next we employ the relation $\xi^2/a_0^2 = b\sqrt{3}/4\pi$ and rewrite $\overline{k_{0,\xi'}} = (1/a_0)\sqrt{4\pi^2 + 8\pi(1-b)/(\sqrt{3}C^2 b)}$. The resulting expression for the total edge potential is:

$$V_{ce,0}(\mathbf{r}) = -\left[\cosh(k_0 y) - \frac{e^{(1-s(b))\pi\frac{w+b_0}{a_0}}}{s(b)} \cosh(k_0 y s(b)) \right]$$
$$\times 2U_0(1-b) e^{-\pi\frac{w+b_0}{a_0}} \cos k_0 x, \qquad \text{(A5)}$$

where $s(b) = \sqrt{1 + (2-2b)/(\pi\sqrt{3}C^2 b)}$.

For a channel with $w = b_0$, the maximum $\mu(b)$ of the sinusoidal pinning force $-\partial_x V_{ce,0}$ at $y = 0$ is then given by:

$$\mu(b) \simeq 2\frac{U_0(1-b)f(b)}{12\pi a_0}, \qquad \text{(A6)}$$

where we used $e^{-\pi\sqrt{3}} \simeq 1/24\pi^2$ and

$$f(b) = 1 - 24\pi^3 \frac{e^{-\sqrt{\frac{\pi\sqrt{3}(2-2b)}{C^2 b} + 3\pi^2}}}{\sqrt{\frac{\pi(2-2b)}{C^2\sqrt{3}b} + \pi^2}}. \qquad \text{(A7)}$$

It can be checked that the associated shear modulus $c_{66} = \pi\sqrt{3}\mu(b)/2a_0$ is very similar to the interpolation

formula of Brandt Eq.(2). Additionally, the edge potential Eq.(A5) is harmonic for all fields. Hence the ideal flow stress of a commensurate, ordered channel, is characterized by Frenkels value $A^0 = 1/\pi\sqrt{3}$ for all fields [66]. In the low field limit $b \lesssim 0.2$ (and $\lambda/a_0 \gtrsim 1/\pi$) the above expressions reduce to Eq.(8), (9) in Sec. III A.

Using the field-dependent vortex interaction Eq.(A2), one can derive the parameters in the sine-Gordon description of Sec. III A generalized for higher field. The equation for the chain stiffness becomes:

$$\kappa_q = U_0 \pi (1-b) \left[\frac{\lambda'/a_0}{\sqrt{1 + \lambda'^2 q^2}} - \frac{\xi'/a_0}{\sqrt{1 + \xi'^2 q^2}} \right]. \quad \text{(A8)}$$

The reduced stiffness is obtained from $g(b) = \kappa_0(b)/(k_0\mu(b)a_0^2)$:

$$g(b) = \frac{3\pi}{f(b)} \sqrt{\frac{\sqrt{3}b}{4\pi(1-b)}} \left(\frac{\lambda}{\xi} - \frac{C}{\sqrt{2}} \right) \qquad \text{(A9)}$$

Taking into account these refinements in Eq.(10) and Eq.(17), the defect width in the nonlocal regime becomes:

$$l_d^{nl}(b) = 6\pi^2 a_0/f(b). \qquad \text{(A10)}$$

One can obtain the typical crossover field b_{nl} (or typical $\lambda/a_{0,nl}$) at which nonlocal behavior sets in for a chain in an ordered channel by equating Eq.(A10) to the s-G value for the kink width $2\pi a_0\sqrt{g(b)}$. Approximating $f(b) \simeq (1-b)$, one finds $1 - b = 3\pi/\sqrt{g(b)}$, which has the approximate solution

$$b_{nl} \simeq \frac{1}{2} \left[1 - \sqrt{1 - (48\sqrt{3}\pi^3\xi^2/\lambda^2)} \right] \qquad \text{(A11)}$$

Hence, the nonlocal regime is absent for a channel in a material with $\lambda/\xi \lesssim 50$ (and thickness $d \gtrsim \lambda$). For $\lambda/\xi \gtrsim 60$, nonlocal behavior occurs for $b > b_{nl}$ with $b_{nl} \lesssim 0.2$. This is to be compared with the estimate $a_{0,nl} < \lambda/3\pi$ resulting from a simple London interaction, see Sec. III A.

APPENDIX B: SOLUTION TO THE DYNAMIC SINE-GORDON EQUATION

For a displacement field of the form Eq.(24), expressed in modes with wave vector $mq = 2\pi mc_d$ and amplitude h_m, Eq.(23) for the v-f curve attains the form:

$$f = \gamma v \left[1 + 2k_0^2 \sum_{m=1}^{M} m^2 |h_m|^2 \right]. \qquad \text{(B1)}$$

The amplitudes h_m are obtained by inserting Eq.(24) into the equation of motion (13) with the wavelength dependent elasticity $\kappa(q)$ from Eq.(12). Since h can become of the order of a lattice spacing a_0, one expands the 'sin' term in (13) up to second order in h. Furthermore, we

assume that h_m decays rapidly upon increasing m and we keep only the three lowest order contributions h_m with $m \leq 3$. Collecting terms of equal wave number, one obtains the following set of approximate equations:

$$\frac{2}{\mu}(i\gamma v k_0 + K_{1,q})h_1 = \quad -i + ik_0^2(|h_1|^2 + |h_2|^2)$$
$$+k_0 h_2 - i(k_0^2/2)h_1^2 \quad (B2)$$

$$\frac{2}{\mu}(2i\gamma v k_0 + K_{2,q})h_2 = k_0 h_1 + ik_0^2(h_1^* h_2 - h_1 h_2) \quad (B3)$$

$$\frac{2}{\mu}(3i\gamma v k_0 + K_{3,q})h_3 = k_0 h_2 + i(k_0^2/2)h_1^2, \quad (B4)$$

where $K_{m,q} = m^2 q^2 \kappa(mq)$ and h^* denotes the complex conjugate of h. At small v, the real components of h vanish and the amplitudes describing the shape of the quasi-static deformations are given by:

$$|h_1| \approx \frac{(2K_{1,q}/\mu) - \sqrt{(2K_{1,q}/\mu)^2 + 6k_0^2}}{3k_0^2} \quad (B5)$$

$$|h_2| \approx \frac{-k_0|h_1|}{2k_0^2|h_1| - (2K_{2,q}/\mu)} \quad (B6)$$

$$|h_3| \approx \frac{\mu(k_0|h_2| - k_0^2|h_1|^2/2)}{2K_{3,q}}. \quad (B7)$$

For arbitrary v, the h_m's in Eq.(B2,B3,B4) may be determined by a mathematical program. However, the most important effect of the coupling is that above a characteristic velocity v^* (see below), $|h_2|$ and $|h_3|$ decrease rapidly as $|h_2| \sim |h_1|/v$ and $|h_3| \sim |h_1|^2/3v$, so that only the first Fourier mode survives. This mode is described by ($v \gg v^*$):

$$h_1(v) \quad = \frac{(2\gamma v/\mu) - \sqrt{(2\gamma v/\mu)^2 + 2}}{k_0}$$
$$\approx -\frac{\mu}{2\gamma v k_0}, \quad (B8)$$

Since Eq.(B8) can be obtained by neglecting the elastic force terms $\kappa_{n,q}$, it describes the deviation from the average velocity of a single particle in a periodic potential. Further analysis of Eq.(B2,B3,B4) shows that the crossover velocity v^* is determined by the amplitude of the quasi-static result in Eq.(B5,B6,B7):

$$(2\gamma v^* k_0/\mu)^2 \sum_{m=1}^{3}(m|h_m|)^2 \approx 1. \quad (B9)$$

Using the definition

$$K_{eff}^2(c_d = \frac{q}{2\pi}) \equiv \frac{\mu^2}{4}\left(\sum_{m=1}^{3}(m|h_m|)^2\right)^{-1}, \quad (B10)$$

we rewrite Eq.(B9):

$$k_0 v^* = K_{eff}(c_d)/\gamma. \quad (B11)$$

Here $\gamma/K_{eff}(c_d)$ can be interpreted as the effective relaxation time for the non linear deformations in the chain, which is expressed through the relaxation times $\gamma/K_{m,q}$ of linear modes (phonons) by Eq.(B10). The velocity dependence of $\sum(m|h_m|)^2$ may then be written as:

$$\sum_{m=1}^{3} m^2 |h_m(v)|^2 = \frac{\mu^2}{4[K_{eff}^2 + (\gamma v k_0)^2]}. \quad (B12)$$

This has the correct small v behavior (where higher modes play a role) and large v behavior (where $h_2 \approx h_3 \approx 0$). First order perturbation using only h_1 to first order in Eq.(B2) yields the same functional form but with K_{eff}^2 replaced by $K_{1,q}^2$, supporting the analytical interpolation made in obtaining Eq.(B12). Finally, using Eq.(B1) one arrives at Eq.(25) in section III B.

APPENDIX C: ELASTIC SHEAR WAVES IN COMMENSURATE, ORDERED CHANNELS

Starting from Eq.(26) we write u as the sum of a spatially uniform dc-component and a non-uniform, time-dependent component $h(y,t)$. The result for $h(y,t) = u(y,t) - vt$ is the following modified diffusion equation:

$$\gamma \partial_t h(y,t) = (f - \gamma v) + c\partial_y^2 h(y,t), \quad (C1)$$

where $c = b_0^2 k_0 \mu/2 = c_{66}a_0 b_0$. The boundary condition is set by:

$$\gamma \partial_t h(-w/2, t) = \quad -(\mu/2)\sin[\omega_0 t + h(-w/2, t)]$$
$$+(c/b_0^2)\Delta h(t), \quad (C2)$$

and similarly for $y = +w/2$. Here the discrete character of the array near the CE's is retained in $\Delta h = h(-w/2 + b_0, t) - h(-w/2, t)$. For the pinning term (last term on the r.h.s.) we now use the large velocity expansion for the restoring force from one CE: $(\mu/2)\sin[k_0(vt + h)] \simeq (\mu/2)\sin[\omega_0 t]$. Then Eqs.(C1),(C2) become similar to those for heat diffusion in a rod with at both ends heat sources that vary sinusoidally in time. In our case the frequency is the washboard frequency $\omega_0 = k_0 v$. By separation of variables one finds:

$$h(y,t) = \quad h_e A_{e,v}(w)[f_v(y)\cos(\omega_0 t) + g_v(y)\sin(\omega_0 t)]$$
$$-\frac{(f - \gamma v)}{2c}y^2, \quad (C3)$$

where $f_v(y) = -\cos(y/l_{\perp,v})\cosh(y/l_{\perp,v})$ and $g_v(y) = \sin(y/l_{\perp,v})\sinh(y/l_{\perp,v})$ with a velocity (frequency) dependent 'healing' length $l_{\perp,v} = \sqrt{2c/\gamma\omega_0} = \sqrt{(\mu/\gamma v)}b_0$. The factor $A_{e,v}(w) = 1/\sqrt{f_v^2(w/2) + g_v^2(w/2)}$ normalizes the displacement at the CE to h_e. The latter is obtained from the boundary condition Eq.(C2). In the limit
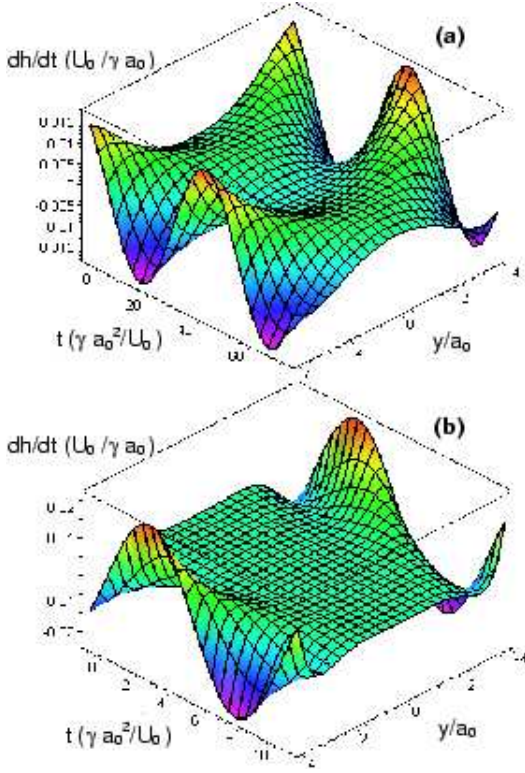
FIG. 31: Velocity profile $\partial_t h(y,t)$ versus time from Eq.(C3) in a channel with $w/b_0 = 9$. (a) for $\gamma v/\mu \simeq 0.4$ and (b) for $\gamma v/\mu \simeq 2$.

$w/b_0 = n \geq 3$ and $\gamma v/\mu \gtrsim 0.25$, h_e can be approximated by:

$$h_e \simeq \frac{\mu}{2k_0 \gamma v} \sqrt{\frac{2\gamma v}{2\gamma v + \mu}} \qquad (C4)$$

The solution (C3) describes a periodic velocity modulation $\partial_t h$ of each chain, with a y-dependent amplitude $|h'|$ and phase shift. The latter reflects periodic lagging and advancing of the inner rows with respect to the outer ones. Both the decay of $|h'|$ away from the CE and the phase shift strongly increase with velocity through $l_{\perp,v}$. In Fig. 31 we have illustrated this behavior for small velocity $\gamma v/\mu = 0.4$ (a) and larger velocity $\gamma v/\mu = 2$ (b). Although the result in (a) is actually out of the regime of validity of the high velocity expansion, the 'in-phase' behavior at small v is a feature that qualitatively agrees with the simulations. For comparison we show in Fig. 32 numerical results for the oscillating velocity component for $w/b_0 = 9$ and small drive, $f \simeq 2f_s \simeq \mu/5$ ($\gamma v/\mu \approx 0.16$). In addition to the small phase shift one observes that the modulation is highly non-sinusoidal, which is not captured by our approximate solution.

Based on the above, one can also evaluate the dynamic friction force $f - \gamma v$. Using Eq.(20),(23), the expression for the elastic-continuum $u(y,t)$ would be $f - \gamma v = (\gamma/vw) \int dy dt [\partial_t h(y,t)]^2$. However, in the velocity regime where our solution applies, the length
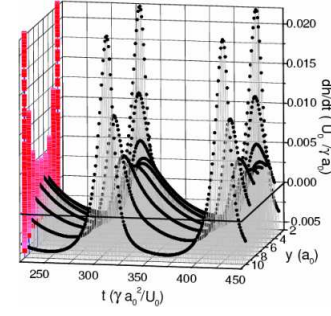
FIG. 32: Simulation result of the profile of the fluctuating velocity component $\partial_t h$ versus time in a channel with $w/b_0 = 9$ at $f = 0.011$. The projection in the $y - dh/dt$ plane further clarifies the y-dependence of $|h'|$.

$l_{\perp,v} \leq 2b_0$. Since we have a discrete number of vortex rows, it is the two outer rows at $y = \pm w/2$ which give the dominant contribution. Evaluating $f - \gamma v$ using Eq.(C4) then leads to Eq.(28) in Sec. IV.

APPENDIX D: DISORDERED CHANNEL POTENTIAL AND PINNING OF DEFECTS

In this appendix we derive the disorder corrections to the channel potential and the effect on pinning of the chain. For the vortex interaction we use the London potential of Eq.(6). Starting from Eq.(30) we first split the potential in contributions from row m with transverse coordinate y:

$$V_m(x) = (2\pi)^{-1} \int dk V(k,y) \rho_m(k) e^{ikx}, \qquad (D1)$$

where $k = k_x$ and

$$V(k,y) = U_0 \pi \frac{e^{-y\sqrt{k^2 + \lambda^{-2}}}}{\sqrt{k^2 + \lambda^{-2}}}. \qquad (D2)$$

In addition, $\rho_m(k)$ in Eq.(D1) is related to the longitudinal displacement field $d_m^x(x)$ via [47]

$$\rho_m(k) = a_0^{-1} \int dx \left[1 - \partial_x d_m + \delta\rho_m(x - d_m)\right] e^{-ikx} \quad (D3)$$

which contains the microscopic density modulation $\delta\rho_m(x - d_m(x)) = \sum_{l \neq 0} \cos(lk_0[x - d_m(x)])$ as well as the density variations $\propto \partial_x d_m$ due to long wavelength deformations. Inserting Eq.(D3) in Eq.(D1) yields a total potential of the form $V_m(x) = V_{l,m}(x) + V_{p,m}(x)$ where

$$V_{l,m}(x) = -a_0^{-1} \int dx' V(x - x', y) \partial_{x'} d_m(x'), \quad (D4)$$

and

$$V_{p,m}(x) = \frac{2}{a_0} \int dx' V(x - x', y) \cos[k_0(x' - d_m)]. \quad (D5)$$

A constant offset arising from the 'DC'part of the density has been omitted in Eq.(D4) and in Eq.(D5) only the $l = \pm 1$ components of the density are taken into account. The latter represents a quasi-periodic potential with wavelength $\sim a_0$. It is only significant for $y \lesssim 1.5 b_0$, i.e. for $m = \pm 1$, as in the pure case. Therefore V_p can be written as

$$V_p = -[\mu + \delta\mu(x)]\cos[k_0(x-d)]/k_0, \quad \text{(D6)}$$

where $d = (d_1 + d_{-1})/2$ and

$$
\begin{aligned}
\delta\mu(x) &= \frac{k_0}{a_0^2}\int dk[V(k_+, b_0) - V(k_-, b_0)]ikd(k)e^{ikx} \\
&\simeq \pi\sqrt{3}\mu\partial_x d, \quad \text{(D7)}
\end{aligned}
$$

where $k_\pm = k_0 \pm k$ and the second line is valid for $k \lesssim 0.4 k_0$. The local strains thus also provide variations in the potential height. A similar conclusion holds when transverse shifts in the CE are included. In the simulations the mean square strain is $\langle(\nabla\cdot\mathbf{d})^2\rangle = \Delta^2/3$ and short range ($\sim a_0/2$) correlated along x with correlator $S(s,0) \equiv \langle\partial_x d(x,y)\partial_x d(x+s, y' = y)\rangle_x \simeq (\Delta^2/3)e^{-(2s/a_0)^2}$. Accordingly, the amplitude fluctuations of the periodic potential are characterized by:

$$\Gamma_a(s) = \frac{\langle\delta\mu(x)\delta\mu(x+s)\rangle_x}{k_0^2} \simeq (\mu\Delta a_0/2)^2 e^{-(\frac{2s}{a_0})^2} \quad \text{(D8)}$$

The non-local contributions Eq.(D4) add up to a total contribution $V_l = \sum_{m\neq 0} V_{l,m}$ in V_{ce}. V_l thus originates from strains within a region $\sim \lambda$ around the channel and will be smooth on the scale a_0 (we assume $\lambda \gg a_0$). Transforming the sum into an integral and using Eq.(D2), the correlator $\Gamma_l = \langle V_l(x)V_l(x+s)\rangle$ can be written as [67]:

$$\Gamma_l(s) = \frac{1}{a_0^4}\int_{CE} dy dy'\int dx A_{y,y'}(x)S(s-x, y'-y) \quad \text{(D9)}$$

The term $A_{y,y'}(x) = (2\pi)^{-1}\int dk V(k,y)V(k,y')\cos(kx)$ can be approximated by

$$A_{y,y'}(x) \simeq U_0^2\pi\lambda e^{-\frac{|y|+|y'|}{\lambda}}e^{-(\frac{x}{\lambda})^2}. \quad \text{(D10)}$$

In case the strains are uncorrelated between the rows $S(x, y'-y) \sim \exp(-(2(x^2+(y'-y)^2)/a_0^2))$ and Eq.(D9) can be approximated by

$$\Gamma_l(s) \simeq C_\alpha\Delta^2 U_0^2(\lambda/a_0)^{1+\alpha}e^{-(\frac{s}{\lambda})^2}, \quad \text{(D11)}$$

with $\alpha = 1$ and $C_1 \simeq 1$. In case of uniform strains, $S(x)$ is independent of $y'-y$. Then again the correlator is given by the above formula, but with $\alpha = 2$ and $C_2 = (4/3)\pi^{3/2}$.

To study the effect of the disorder on the pinning of vortices inside the channel, we write the total energy as a sum of an elastic and a pinning term:

$$H(x,u) = H_{el} + H_p = a_0^{-1}\int dx\frac{\kappa_0}{2}(\partial_x u)^2 + H_p. \text{(D12)}$$

The dispersion of the elastic constant has been neglected and u represents the displacements of vortices inside the channel. By writing the density of the chain as $\rho_c(x,u) = a_0^{-1}[1 - \partial_x u + \sum_{l\neq 0}\cos(lk_0(x-u))]$, the pinning term H_p in Eq.(D12) can be expressed as:

$$H_p = a_0^{-1}\int dx(V_p + V_l)(\delta\rho(x,u) - \partial_x u), \quad \text{(D13)}$$

where only the lowest Fourier components of ρ_c are retained, i.e. $\delta\rho(x,u) = 2\cos k_0(x-u)$. This expression can be simplified as follows. Since we consider the limit where $\partial_x u$ is nearly constant within a_0, the cross-term of the quasi-periodic potential V_p and $\partial_x u$ can be neglected compared to the $V_l(x)\partial_x u$ term. The product $V_l\delta\rho(x,u)$ is also oscillatory and can be neglected as well [68]. The other remaining term $V_p(x)\delta\rho(x,u)$ can be written as $(\mu(x)/k_0)\cos[k_0(u-d)]$. Shifting the argument via $k_0(u-d) = k_0\tilde{u}$ and writing $\tilde{u} \to u$, an extra term $\kappa_0\partial_x d\partial_x u$ is generated in H_{el} in Eq.(D12) (and also u-independent terms which can be neglected). The total coupling to the strain $\partial_x u$ then consists of $V_s \equiv V_l - \kappa_0\partial_x d$. The result for the total energy is

$$H = H_{SG} - \int\frac{dx}{a_0}\left[\frac{\delta\mu(x)}{k_0}\cos(k_0 u) - V_s(x)\partial_x u\right] \text{(D14)}$$

The potential V_s has a correlator $\langle V_s(x)V_s(x+s)\rangle = \Gamma_s(s)$ which is characterized by

$$\Gamma_s(s) = \frac{16\pi^2 g^2}{3}\Gamma_a(s) + \Gamma_l(s) + \frac{2U_0\Delta^2\lambda}{a_0}V(s, b_0) \text{(D15)}$$

in which $g = \kappa_0/(2\pi\mu a_0)$ and the last term arises from cross-correlations. In Eq.(D14), $H_{SG} = \int dx[(\kappa_0/2)(\partial_x u)^2 - (\mu/k_0)\cos(k_0 u)]$ is the original sine-Gordon energy functional of the pure model and the remaining terms reflect the corrections due to disorder. Finally, we denote the first correction, which is due to the amplitude fluctuations, as H_a and the second, coupling to the strain, as H_s.

For weak disorder, we can now calculate the effect of disorder on a defect in the chain by assuming that the shape of a defect at x, $u_d(x'-x) = 2a_0\arctan[\exp(\pm 2\pi(x'-x)/l_d)]/\pi$, is unchanged by disorder [49]. The pinning energy of a defect due to the term H_a is:

$$E_a(x) = (a_0 k_0)^{-1}\int dx'\delta\mu(x')\cos(k_0 u_d(x'-x)) \text{(D16)}$$

The correlations of E_a are given by [67]:

$$\langle E_a(x)E_a(x+s)\rangle = \frac{1}{a_0^2}\int dp A_a(p)\Gamma_a(s-p), \quad \text{(D17)}$$

where

$$A_a(p) = \int\frac{4(l_d/2\pi)d\tilde{x}}{\cosh^2(\tilde{x})\cosh^2(\tilde{x}+\tilde{p})} \simeq l_d e^{-(\frac{4p}{l_d})^2}, \quad \text{(D18)}$$

with $\tilde{x} = 2\pi x/l_d$. For $l_d \gg a_0$ we can approximate $\Gamma_a(s)$ in Eq.(D17) by $\Gamma_a(s) \simeq (\mu\Delta)^2(\sqrt{\pi}a_0^3/8)\delta(s)$ leading to:

$$\langle E_a(x)E_a(x+s)\rangle = (\sqrt{\pi}/8)\mu^2\Delta^2 l_d a_0 e^{-(\frac{4s}{l_d})^2}. \quad \text{(D19)}$$

The effect of the coupling to the strain is given by $E_s(x) = (a_0)^{-1}\int dx' V_s(x')\partial_x u_d(x'-x)$ which has the following correlator:

$$\langle E_s(x)E_s(x+s)\rangle = \frac{1}{a_0^2}\int dp A_s(p)\Gamma_s(s-p). \quad \text{(D20)}$$

Using $\partial_x u_d = (2a_0/l_d)\cosh^{-1}(2\pi x/l_d)$, A_s is given by:

$$A_s(p) = \int \frac{(2a_0^2/\pi l_d)d\tilde{x}}{\cosh(\tilde{x})\cosh(\tilde{x}+\tilde{p})} \simeq \frac{4a_0^2 e^{-(\frac{2p}{l_d})^2}}{\pi l_d}. \quad \text{(D21)}$$

For $l_d \gtrsim \lambda$ the final result is:

$$\langle E_s(x)E_s(x+s)\rangle \simeq \frac{(U_0\Delta\lambda)^2}{l_d a_0}[C_l+4]e^{-(\frac{2s}{l_d})^2}, \quad \text{(D22)}$$

where the term $C_l \simeq 2C_\alpha(\lambda/a_0)^\alpha$ in square brackets is due to the nonlocal contribution V_l and the factor 4 arises from the term $\sim \partial_x d$ in V_s. Hence, for large λ/a_0 the nonlocal term dominates in the coupling to the strain.

[1] G. Blatter *et al.*, Rev. Mod. Phys. **66**, 1125, (1994).
[2] G. Grüner, Rev. Mod Phys. **60**, 1129 (1988).
[3] B.N.J. Persson, *Sliding Friction: Physical Principles and Applications* (Springer-Verlag, Berlin, 1998).
[4] Y.P. Li, T. Sajoto, L.W. Engel, and D.C. Tsui, Phys. Rev. Lett. **67**, 1630 (1991); M. Cha and H.A. Fertig, Phys. Rev. B **50**, 14368 (1994).
[5] R. Seshadri and R.M. Westervelt, Phys. Rev. Lett. **70**, 234 (1993); R. Seshadri and R.M. Westervelt, Phys. Rev. B **47**, 8620 (1993).
[6] M. Baert, V. V. Metlushko, R. Jonckheere, V. V. Moshchalkov, and Y. Bruynseraede, Phys. Rev. Lett **74** 3269 (1995).
[7] J. I. Martn, M. Vlez, A. Hoffmann, I. K. Schuller, and J. L. Vicent, Phys. Rev. Lett. **83**, 1022 (1999).
[8] W. K. Kwok, U. Welp, G. W. Crabtree, K. G. Vandervoort, R. Hulscher, and J. Z. Liu, Phys. Rev. Lett. **64**, 966 (1990); W. K. Kwok, U. Welp, V. M. Vinokur, S. Fleshler, J. Downey, and G. W. Crabtree, Phys. Rev. Lett. **67**, 390 (1991);
[9] H.J. Jensen, A. Brass, and A. J. Berlinsky, Phys. Rev. Lett. **60**, 1676 (1988); H. J. Jensen, A. Brass, Y. Brechet, and A. J. Berlinsky, Phys. Rev. B **38**, 9235 (1988).
[10] A.C. Shi and A.J. Berlinsky, Phys. Rev. Lett. **67**, 1926 (1991).
[11] M. Marchevsky, J. Aarts, and P.H. Kes, Phys. Rev. B **60**, 14601 (1999).
[12] F. Pardo, F. De La Cruz, P.L. Gammel, C.S. Oglesby, E. Bucher, B. Batlogg, and D.J. Bishop, Phys. Rev. Lett. **78**, 4633 (1997).
[13] F. Pardo, F. de la Cruz, P.L. Gammel, E. Bucher, and D.J. Bishop, Nature **396**, 348 (1998).
[14] A.I. Larkin, Zh. Eksp. Teor. Fiz. **58**, 1466 (1970); A.I. Larkin and Yu. Ovchinikov, J. Low Temp. Phys. **34**, 409 (1979).
[15] P.H. Kes and C.C. Tsuei, Phys. Rev. Lett. **47**, 1930 (1981); Phys. Rev. B **28**, 5126 (1983).
[16] R. Wördenweber and P.H. Kes, Phys. Rev. B **34**, 494 (1986).
[17] A.M. Troyanovski, M. van Hecke, N. Saha, J. Aarts, and P.H. Kes, Phys. Rev. Lett. **89**, 147006 (2002).
[18] A. P. Mehta, C. Reichhardt, C. J. Olson, and F. Nori, Phys. Rev. Lett. **82**, 3641 (1999); C.J. Olson, C. Reichhardt, and F. Nori, Phys. Rev. Lett. **81**, 3757 (1998).
[19] S. Ryu, M.C. Hellerqvist, S. Doniach, A. Kapitulnik, and D. Stroud, Phys. Rev. Lett. **77**, 5114 (1996).
[20] M.C. Hellerqvist, D.Ephron, W.R. White, M.R. Beasley, and A. Kapitulnik, Phys. Rev. Lett. **76**, 4022 (1996); M. Danckwerts, A. R. Goi, and C. Thomsen, Phys. Rev. B **59**, 6624 (1999).
[21] O. Daldini, P. Martinoli, J. L. Olsen, and G. Berner, Phys. Rev. Lett. **32**, 218 (1974).
[22] P. Martinoli, Phys. Rev. B **17**, 1175 (1978).
[23] K. Harada, O. Kamimura, H. Kasai, T. Matsuda, A. Tonomura, and V. V. Moshchalkov, Science **274**, 1167 (1996). M. Velez, D. Jaque, J. I. Martn, M. I. Montero, I. K. Schuller, and J. L. Vicent, Phys. Rev. B **65**, 104511 (2002).
[24] E. Rosseel, M. Van Bael, M. Baert, R. Jonckheere, V. V. Moshchalkov, and Y. Bruynseraede, Phys. Rev. B **53**, 2983 (1996); L. Van Look, E. Rosseel, M. J. Van Bael, K. Temst, V. V. Moshchalkov, and Y. Bruynseraede, Phys. Rev. B **60**, 6998 (1999).
[25] C. Reichhardt, C.J. Olson, and F. Nori, Phys. Rev. Lett. **78**, 2648 (1997); C. Reichhardt, C.J. Olson, and F. Nori, Phys. Rev. B **58**, 6534 (1998); C. Reichhardt, G. T. Zimnyi and N. Gronbech-Jensen, Phys. Rev. B **64**, 014501 (2001).
[26] D. Dew-Hughes, Phil. Mag. B **4**, 459 (1987).
[27] A. Pruymboom. Ph.D. Thesis, Leiden University (1988).
[28] A. Gurevich, Phys. Rev. B **46**, 3187 (1992); Phys. Rev. B **65**, 214531 (2002); A. Gurevich, M. S. Rzchowski, G. Daniels, S. Patnaik, B. M. Hinaus, F. Carillo, F. Tafuri, and D. C. Larbalestier, Phys. Rev. Lett. **88**, 097001 (2002).
[29] A. Pruymboom, P.H. Kes, E. van der Drift, and S. Radelaar, Phys. Rev. Lett. **60**, 1430 (1988); M.H. Theunissen, E. van der Drift, and P.H. Kes, Phys. Rev. Lett. **77**, 159 (1996).
[30] E.H. Brandt, J. Low Temp. Phys. **26**, 709 (1977); *ibid.* **26**, 735 (1977); J. Low Temp. Phys. **28**, 263 (1977); *ibid.* **28**, 291 (1977); Phys. Stat. Sol. (b) **77**, 551 (1976).
[31] N. Kokubo, R. Besseling, V.M. Vinokur, and P.H. Kes, Phys. Rev. Lett. **88**, 247004 (2002).

[32] N. Kokubo, R. Besseling, and P.H. Kes, Phys. Rev. B **69**, 064504 (2004).

[33] R. Besseling, T. Dröse, V. M. Vinokur and P. H. Kes, Europhys. Lett. **62**, 419 (2003).

[34] G.J.C. van Baarle, A.M. Troianovski, T. Nishizaki, P.H. Kes and J. Aarts, Appl. Phys. Lett. **82**, 1081 (2003).

[35] R. Besseling, R. Niggebrugge and P.H. Kes, Phys. Rev. Lett. **82**, 3144 (1999).

[36] J. Frenkel, Z. Phys. **37**, 572 (1926).

[37] A.E. Koshelev and V.M. Vinokur, Phys. Rev. Lett. **73**, 3580 (1994).

[38] C.S. Owen and J. Scalapino, Phys. Rev. **164**, 538 (1967).

[39] M. Büttiker and R. Landauer, Phys. Rev. A. **23**, 1397 (1981).

[40] O.M. Braun and Yu.S. Kivshar, Phys. Rep. **306**, 1 (1998).

[41] M. Tinkham, *Introduction to Superconductivity* McGRAW-HILL INTERNATIONAL EDITIONS, 1996.

[42] O.M. Braun, Yu.S. Kivshar and I.I. Zelenskaya, Phys. Rev. B. **41**, 7118 (1990); O.M. Braun and Y.S. Kivshar, Phys. Rev. B **50**, 13388 (1994); S.F. Mingaleev, Y.B. Gaididei, E. Majernikova, and S. Shpyrko, Phys. Rev. E **61**, 4454 (2000).

[43] Practically, discreteness effects can be neglected for $g \gtrsim 2$. One can then also consider the regime $\lambda/a_0 \lesssim 1$. The reduced stiffness is $g = V''(x = a_0)/V''_{ce,0}$ where $V''(x = a_0) \simeq (U_0/\lambda^2)\sqrt{\pi\lambda/(2x)}e^{-x/\lambda}(1 + \lambda/x)$ and V''_{ce} is obtained from the full (λ dependent) expression for $V_{ce,0}$ in App. A (Eq.(A3) and (A4)). The result is that the continuum approach is valid for $\lambda/a_0 \gtrsim 0.3$. For the frequently occurring geometry of a vortex chain confined by vortices pinned in a square array one can also estimate the continuum regime. In this case one replaces $(w+b_0)/2$ in Eq.(8) by $a_0/2$, yielding a periodic pinning force with $\mu_\square \simeq 10\mu$. Correspondingly $g_\square \simeq \lambda/a_0$ and lattice discreteness is unimportant for $\lambda/a_0 \gtrsim 2$.

[44] T. Strunz and F. Elmer, Phys. Rev. E **58**, 1601 (1998).

[45] P. Ziswiler, V. Geshkenbein, and G. Blatter, Phys. Rev. B **56**, 416 (1997).

[46] D. Cule and T. Hwa, Phys. Rev. B **57**, 8235 (1998).

[47] T. Giamarchi and P. Le Doussal, Phys. Rev. B **52**, 1242 (1995).

[48] B.A. Malomed, Phys. Rev. B **39**, 8018 (1989).

[49] V.M. Vinokur and A.E. Koshelev, Sov. Phys. JETP **70**, 547 (1990).

[50] M.V. Feigelman and V.M. Vinokur, Solid State Communications, **45**, 595 (1983); *ibid.*, **45**, 599 (1983); V.M. Vinokur and M.B. Mineev, Sov. Phys. JETP **61** 1073 (1985).

[51] H. Fukuyama and P.A. Lee, Phys. Rev. B **17**, 535 (1978); P.A. Lee and T.M. Rice, Phys. Rev. B **19**, 3970 (1979); an early study of the competition between impurity and commensurability pinning was reported in H. Fukuyama, J. Phys. Soc. Japan **45**, 1474 (1978).

[52] L. Chen *et al.*, Phys. Rev. B **54**, 12798 (1996).

[53] J. Krug, Phys. Rev. Lett. **75**, 1795 (1995).

[54] L. Balents and M.P.A Fisher, Phys. Rev. Lett. **75**, 4270 (1995).

[55] The convective term $-\gamma v\partial_x u \simeq -f\partial_x u$ arises naturally when realizing that the driving force density on a 'string' segment is the product of f and the average vortex density $\sim (1 - \partial_x u)$, see also [46].

[56] C.R. Myers and J.P. Sethna, Phys. Rev. B **47**, 11171 (1993); D. Cule and T. Hwa, Phys. Rev. Lett. **77**, 278 (1996).

[57] A detailed study of the *v-f* curves at strong disorder showed that the friction force $f - \gamma v$ exhibited, besides the usual decrease on increasing v above threshold, a shallow minimum and then a weak *increase* when further increasing v. These features did not depend on system size or simulation time step and varied little with commensurability. The observed behavior is in marked contrast with analytical and numerical studies in standard CDW models, which find a correction $f - \gamma v \propto v^{-1/2}$ at large velocity for a 1D system, see L. Sneddon, M.C. Cross, and D.S. Fisher, Phys. Rev. Lett. **49**, 292 (1982) and also H. Matsukawa, J. Ph. Soc. Jap. bf 56, 1522 (1987); **57** 3463 (1988). The difference could arise from the additional u independent random force or the remaining (relatively small) commensurability pinning which are present in our system, but absent in the previous studies. This issue deserves further investigation.

[58] H. Fangohr, S. J. Cox, and P. A. J. de Groot, Phys. Rev. B **64**, 064505 (2001).

[59] The data in Fig. 2 have been taken in a 'field down' experiment. Qualitatively similar data were obtained in 'field cooled' experiments and both data can be interpreted in terms of strong edge disorder. The results of 'field up' measurements however are qualitatively different and indicate much weaker CE disorder in this case, see N. Kokubo *et al.*, in preparation.

[60] A.B. Kolton, D. Dominguez, and N. Gronbech-Jensen, Phys. Rev. Lett. **83**, 3061 (1999).

[61] For the numerical data, f_s was obtained from a criterion $\gamma v/\mu \approx 0.025$, i.e. $\gamma v a_0/U_0 \approx 0.001$, while in the experiments a criterion $v/a_0 = 1$ MHz was used for the critical current. The latter corresponds to a dimensionless criterion $(v/a_0)(\gamma a_0^2/U_0) \simeq (v/a_0)(20\pi\mu_0\lambda^2 B_{c2}/(\sqrt{3}B\rho_0))$ where $\rho_f \simeq 0.2B\rho_0/B_{c2}$ was used, with ρ_0 the normal resistivity and B_{c2} the upper critical field. Taking $\lambda = 1.1$ μm, $B \simeq 0.012(w/b_0)^2$ T for the channel system under investigation, $B_{c2} = 1.55$ T and $\rho_0 = 2$ $\mu\Omega$m, yields $(v/a_0)(\gamma a_0^2/U_0) \simeq 3.4 \cdot 10^{-9}(v/a_0)/(w/b_0)^2 = 3.4\cdot10^{-3}/(w/b_0)^2$. Occasional checks using the latter criterion however yielded results for f_s and A/A^0 essentially the same as in Figs. 25 and 30.

[62] There are several possible explanations for the discrepancy between A_{exp} and the numerical result for A. The experimental system consists of channels with walls of finite hight at the CE's. Screening currents along these walls may cause the average distance between the first mobile row and the first pinned rows to be larger than that in the simulation (where it is b_0 at matching), leading to an overall reduced value of the shear interaction. In addition, the precise amount of disorder in the experimental system is unknown (imaging studies only exist on related geometries and outside the relevant field regime, see B.L.T. Plourde, D.J. Van Harlingen, N. Saha, R. Besseling, M.B.S. Hesselberth, and P.H. Kes, Phys. Rev. B **66**, 054529 (2002) and M.V. Marchevsky, Ph.D. Thesis, Leiden University (1997)). Further, differences in the amount of longitudinal and transverse positional disorder may exist. Finally, compared to the experiments, the simulations were performed for relatively small ratio λ/a_0.

[63] In the experiments we found that the switching point

$n \rightarrow n \pm 1$ together with the maxima and minima in J_s can be shifted to different magnetic field by changing the field history. This implies a non-trivial relation between the effective width w and the physical channel width w_{etched}, depending on the amount of screening currents along the channel walls, see N. Kokubo, R. Besseling and P.H. Kes, Physica C **412-414**, 362 (2004).

[64] M.C. Faleski, M.C. Marchetti, and A.A. Middleton, Phys. Rev. B **54**, 12427 (1996).

[65] R. Besseling, N. Kokubo and P.H. Kes, Phys. Rev. Lett. **91**, 17702 (2003).

[66] Note that this calculation neglects fluctuation effects at high field.

[67] We employed the fact that for a function of the form $R(x) = \int dx' f(\pm(x' - x))g(x')$ the correlator is given by $\langle R_x R_{x+s} \rangle = \int dp A_f(p) \langle g(x)g(x + s \pm p) \rangle$ with $A_f(p) = \int dx' f(x')f(x' + p)$.

[68] One can calculate that the typical correction $E_{b,l}$ to the pin energy of a defect due to a 'backward' scattering term $\int V_l(x) \cos[k_0(x - u_d)]$ vanishes rapidly with increasing λ, i.e. $\langle E_{b,l}^2 \rangle \simeq U_0^2 \Delta^2 g^{1/2} (\lambda/a_0)^{2+\alpha} e^{-(\pi\lambda/a_0)^2}$.